

# Mixed-sediment transport modelling in Scheldt estuary with a physics-based bottom friction law

Qilong Bi · Erik A. Toorman

Received: 9 July 2014 / Accepted: 4 February 2015 / Published online: 10 March 2015  
© Springer-Verlag Berlin Heidelberg 2015

**Abstract** In this study, the main object is to investigate the performance of a few new physics-based process models by implementation into a numerical model for the simulation of the flow and morphodynamics in the Western Scheldt estuary. In order to deal with the complexity within the research domain, and improve the prediction accuracy, a 2D depth-averaged model has been set up as realistic as possible, i.e. including two-way hydrodynamic-sediment transport coupling, mixed sand–mud sediment transport (bedload transport as well as suspended load in the water column) and a dynamic non-uniform bed composition. A newly developed bottom friction law, based on a generalised mixing-length (GML) theory, is implemented, with which the new bed shear stress closure is constructed as the superposition of the turbulent and the laminar contribution. It allows the simulation of all turbulence conditions (fully developed turbulence, from hydraulic rough to hydraulic smooth, transient and laminar), and the drying and wetting of intertidal flats can now be modelled without specifying an inundation threshold. The benefit is that intertidal morphodynamics can now be modelled with great detail for the first time. Erosion and deposition in these areas can now be estimated with much higher accuracy, as well as their contribution to the overall net fluxes. Furthermore, Krone’s deposition law has been adapted to sand–mud

mixtures, and the critical stresses for deposition are computed from suspension capacity theory, instead of being tuned. The model has been calibrated and results show considerable differences in sediment fluxes, compared to a traditional approach and the analysis also reveals that the concentration effects play a very important role. The new bottom friction law with concentration effects can considerably alter the total sediment flux in the estuary not only in terms of magnitude but also in terms of erosion and deposition patterns.

**Keywords** Sediment transport · Mixed sediment · Generalised mixing-length theory · Bottom friction · Near-bottom sediment transport · Residual sediment transport

## 1 Introduction

The Scheldt estuary comprises an area of approximately 21,863 km<sup>2</sup> and is situated in the north-east of France, the west of Belgium and the south-west of The Netherlands, where it is inhabited by about 10 million people (477 inhabitants/km<sup>2</sup>) (Fig. 1). The river is 350 km long, and the water level difference between source and mouth is only 100 m, making it a typical lowland river system with low current velocities and thus meanders. The estuary is defined as the part of the river basin with a tidal influence. It is categorised as the main transition zone or ecotones between the riverine and marine habitats. The Scheldt estuary is open to the southern North Sea and extends 160 km in length from the mouth at Vlissingen to Ghent, where sluices impair the tidal wave in the Upper Scheldt. The tidal wave also penetrates most of the upstream areas, entering the major tributaries Rupel and Durme, resulting in approximately 235 km of tidal river in the estuary. The Scheldt estuary consists of an approximately 60 km long fresh water tidal zone stretching from near the mouth of

---

Responsible Editor: Earl Hayter

This article is part of the Topical Collection on the *12th International Conference on Cohesive Sediment Transport in Gainesville, Florida, USA, 21–24 October 2013*

---

Q. Bi (✉) · E. A. Toorman  
Hydraulics Laboratory, Department of Civil Engineering, KU  
Leuven, Kasteelpark Arenberg 40, Box 2448, 3001 Leuven, Belgium  
e-mail: qilong.bi@bwk.kuleuven.be

E. A. Toorman  
e-mail: erik.toorman@bwk.kuleuven.be

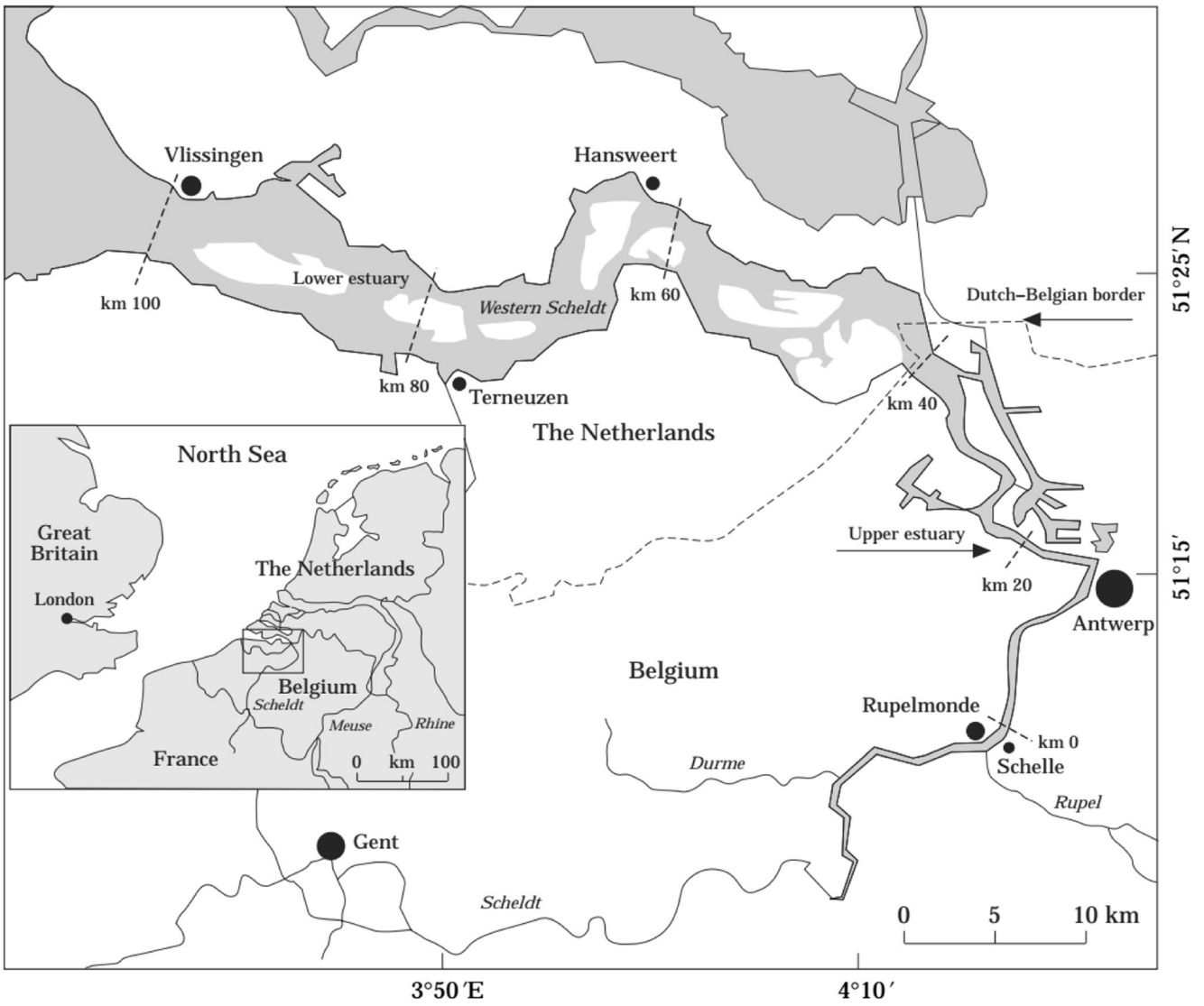


**Fig. 1** The Scheldt estuary. The mixing zone consists of the *upper estuary* and the *lower estuary* or Western Scheldt. Upstream of Rupelmonde the water is entirely fresh, while the water movement is

still dominated by the tide. The area between Rupelmonde and Gent is therefore called the freshwater estuary (from Verlaan et al. 1998)

**Fig. 2** Bathymetry (m) and mesh of the Scheldt estuary

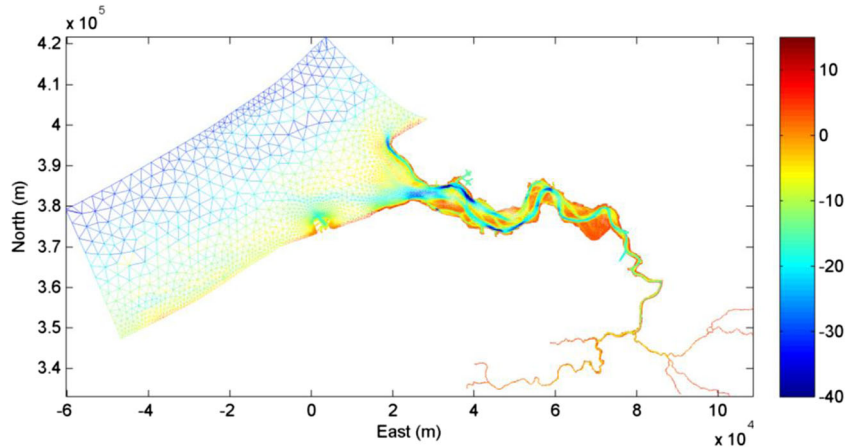
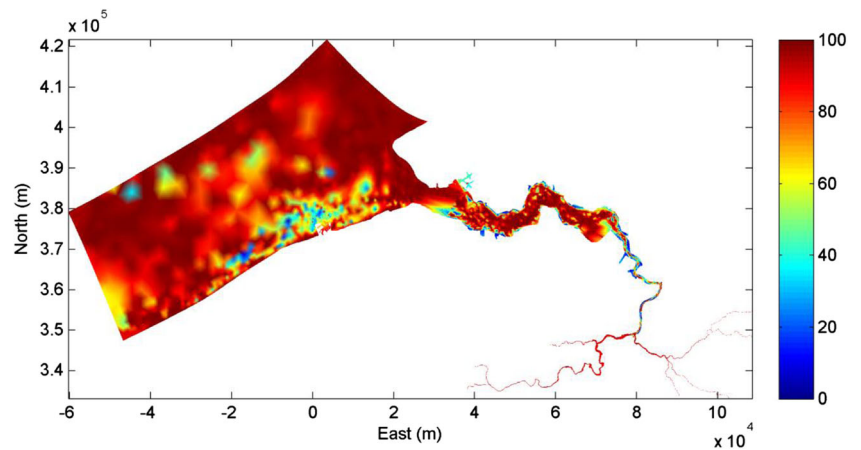


**Fig. 3** Sand fraction distribution map in the Scheldt Estuary (combined data from Rijkswaterstaat, The Netherlands, and RBINS-MUMM, Belgium)



Rupelmonde to Ghent, representing one of the largest freshwater tidal areas in Western Europe. It also has a mixing zone between Rupelmonde and Vlissingen/Breskens. The subtidal delta, seaward of Vlissingen and Breskens, forms the transition between the Western Scheldt and the North Sea (Fettweis et al. 1998; Kuijper et al. 2004; Meire et al. 2005; van Kessel et al. 2011).

The Scheldt estuary can also be divided into two major parts, the Zeeschelde (105 km), which is the Belgian part from Ghent to the Dutch/Belgian boarder, and the Westerschelde (58 km), known as the Dutch part, covering the middle and lower estuary. The Zeeschelde is mainly a single ebb/flood channel and has a total surface of 44 km<sup>2</sup>. Mudflats and marshes in this area are relatively small and approximately account for 28 % of total surface. The Zeeschelde hosts one of the largest harbours in Europe—the Port of Antwerp. Therefore, human activities are very active in this region, and industrial developments are concentrated along the riverbanks. The intertidal zone is often missing or very narrow. The estuary is almost completely canalised upstream of Dendermonde (Hoffmann and Meire 1997). The Westerschelde is a well-mixed region. Due to the influences of tidal waves and land changes, the Westerschelde has a complex and dynamic morphology. The flood and ebb channels are interconnected, bordered by several large intertidal flats and salt marshes. The surface of the Westerschelde amounts to 310 km<sup>2</sup>, in which 35 % of the area is covered by intertidal flats. The average channel depth is approximately 15–20 m (Meire et al. 2005).

In a meso-tidal estuary like the Western Scheldt, where both in- and outflow discharges are large, the net sediment budget is the sum of a large positive and a large negative number. A good knowledge of the sediment budget and transport path is not only essential for longer term planning of maintenance dredging activities, it is also of crucial importance for the impact assessment on and the long-term prediction of the ecosystem services. However, sediment fluxes are very difficult to measure. It requires simultaneous flow and sediment concentration measurements across different cross-sections of the river, in both horizontal and vertical directions. Sediment concentration and flow measurements close to the bottom, where the largest sediment concentrations occur, are particularly difficult and therefore very rare or non-existent. The estimates of the net sediment balance are therefore largely uncertain. Numerical models can help to look at the sediment processes, such as areas of erosion and deposition, but are in need of quantitative measurements for calibration and verification. The bottom friction parameter in these models often, if not always, is the main parameter to calibrate or ‘tune’ the hydrodynamic model, but this also has consequences on the behaviour of the sediment transport model. An additional complication is the fact that sediments are not homogeneous, neither in space nor in time. Transport models that incorporate the possibility to deal with more than one sediment type or class are necessary and available, but the composition of the actual bed is not or at most only partially known. Another important aspect is that the geometry of an estuary is usually complex due to its geomorphological features or water

**Table 1** The properties of the non-cohesive and cohesive sediment

| Type of sediment    | Diameter (μm) | Density (kg/m <sup>3</sup> ) | Settling velocity (m/s) | Critical shear stress for erosion (first layer) (Pa) | Critical shear stress for erosion (second layer) (Pa) |
|---------------------|---------------|------------------------------|-------------------------|--|---|
| Non-cohesive (sand) | 300           | 2650                         | 0.01                    | 0.6  | 0.6   |
| Cohesive (mud)      | 60            | 1600                         | 0.001                   | 0.5  | 0.8   |

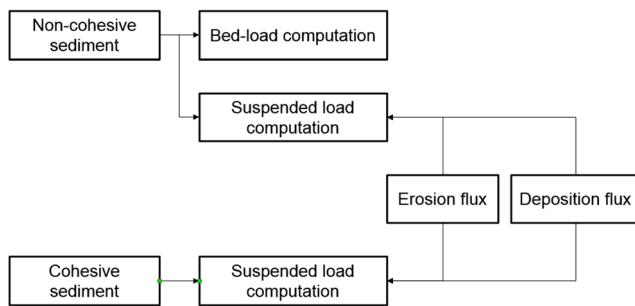


**Fig. 4** Schemes of modelling mixed-sediment transport

circulation patterns. It may also include tidal flats, harbours or navigation channels, which are much smaller compared to the rest of the domain; thus, it requires a more flexible numerical approach to be capable of dealing with all the geometrical complexities.

Many numerical studies have been conducted for understanding hydrodynamics and morphological processes in Scheldt estuary. One of the earliest numerical models for the Scheldt estuary was devised by Baeyens et al. (1981) in order to simulate the physical behaviour, including instantaneous water levels and mean velocities over depth, salinity and turbidity in the water column and the sedimentary budget at the bottom. It was a two-dimensional (2D) depth-averaged model with a structured grid based on a multi-operational finite difference scheme. Later, more efforts were put into the numerical modelling by other researchers and many 2D applications in the Scheldt estuary for simulating sediment transport can be found in studies of Mulder et al. (1990), Portela and Neves (1994), Verbeek et al. (1998), Dam et al. (2007), Bolle et al. (2010), de Brye et al. (2010), and Gourgue et al. (2013). Most of them only focus on the cohesive sediment or mud transport under different hydrodynamic and salinity conditions. However, one of the trends is that the finite element method has been more and more used in the numerical modelling since it is capable of dealing with complex geometry of the estuaries like the Scheldt with a more flexible unstructured mesh. The first three-dimensional (3D) numerical sediment transport model of the Scheldt estuary seems introduced by

**Fig. 5** Critical shear stress for erosion as function of the mud fraction

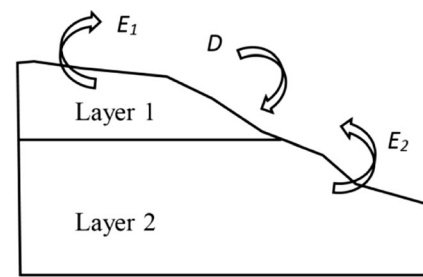
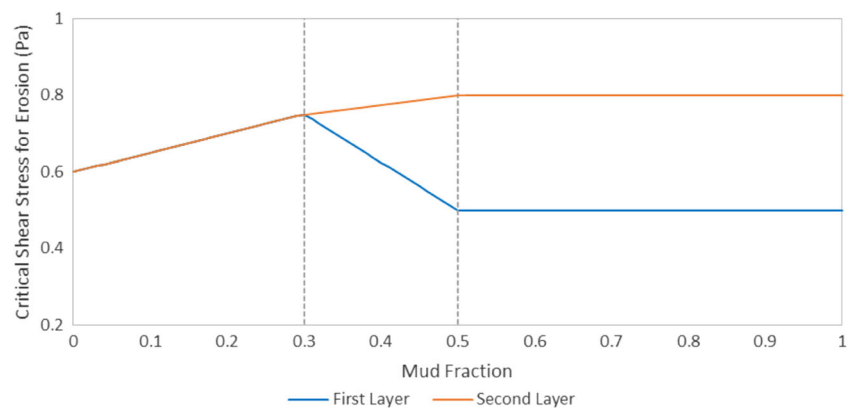


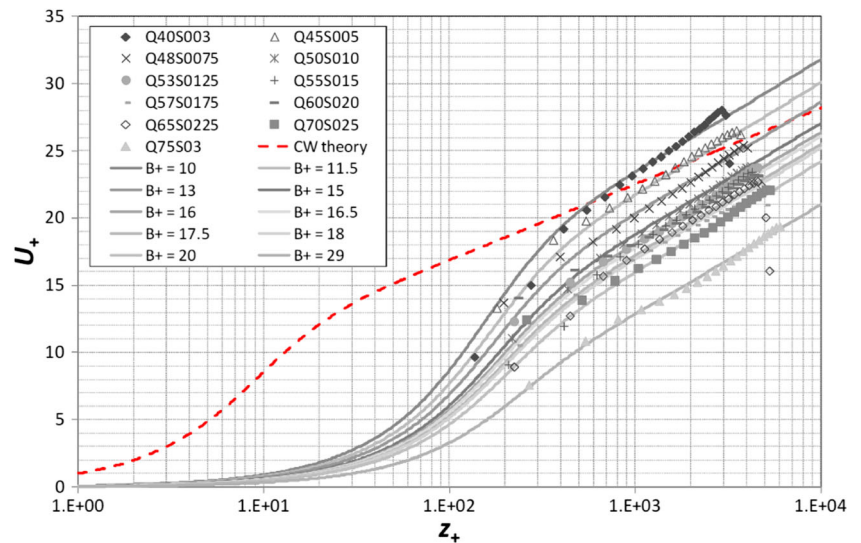
**Fig. 6** Two-layer bed model

Cancino and Neves (1994, 1999a, b). It was a fully 3D finite difference baroclinic model system for hydrodynamics and fine suspended sediment transport with the effects of flocculation, deposition and erosion taken into account. Their approach provided a useful basis for a good understanding of the physical processes involved in sediment transport. Another 3D mud transport model was established by Van Kessel et al. (2011). Their model showed realistic values for water levels, salinities and residual currents in the major part of the model domain. However, the propagation of the tidal wave was modelled less accurately upstream of Antwerp. One of the advantages of a 3D model is that it can reproduce many complex hydrodynamic processes in the estuary under tidal waves. Therefore, it is also a useful tool for studying the effects of secondary currents in the estuary (Verbeek et al. 1998). But also due to its complexities, the computational cost for a 3D large-scale model is much higher than a 2D model.

The purpose of this study was to test and demonstrate a new modelling methodology that was developed to deal with the complexities of large-scale domains like the Scheldt estuary by taking sub-grid-scale physical processes or effects into account, while still trying to maintain the computational efficiency. By including new empirical parameters into physics based laws or criteria, the model can adapt to different situations or scenarios by its own and achieve higher prediction accuracy. Another objective of this study was to make a more realistic model that not only focusses on the cohesive particles but also has non-cohesive sediment in the system. The reason for considering more than one sediment class in the system is



**Fig. 7** Velocity profile for sand-laden turbulent open-channel flow. Flume data for a sand suspension from Cellino (1998) with increasing sediment load, matched with the generalized mixing-length model. *Symbols* measurements, *full lines* calculations, *dashed line* velocity profile for clear water (CW). For this set of experiments,  $\kappa_s=0.27$  (Toorman 2003)



that, in the real world, the bed material consists both cohesive and non-cohesive sediments, and its composition differs from one location to another. For example, according to the measurement carried out in Western Scheldt, one can find the mud fraction in the upstream is generally larger than the values found in the downstream. For each type of sediment, the transport mechanism is different and both transport progresses consume energy. From this perspective, the availability of energy to transport sediments in the system is likely to be overestimated when only considering one type of sediment, or, stated differently, the same energy is used twice. The corresponding error is compensated by tuning the model.

## 2 The mathematic model

The Scheldt model consists of a coupled 2D hydrodynamic model and a 2D sediment transport model, both of them were developed using the OpenTELEMAC-MASCARET modelling system with customisations in the source code. The year

2009 has been selected as the simulation period. According to the study of De Ruijter et al. (1987), the water column in the Belgian coastal zone is well mixed throughout the entire year; therefore, a 2D depth-averaged model is appropriate.

### 2.1 Hydrodynamic model

The development of the hydrodynamic model is based on TELEMAC-2D (TELEMAC-MASCARET, 2013), which is a finite element solver for use in the field of 2D free-surface flows. It has been used in many studies and research cases (Hervouet and Bates 2000). The Navier–Stokes equations for incompressible flow are averaged vertically by integration from the bottom to the surface and solved simultaneously in TELEMAC-2D code using the finite-element method, as well as the equation for tracer conservation (Hervouet 2007).

Continuity equation:

$$\frac{\partial h}{\partial t} + \frac{\partial(hu)}{\partial x} + \frac{\partial(hv)}{\partial y} = 0 \tag{1}$$

**Fig. 8** Chézy coefficients obtained from the new bottom friction law with concentration effects

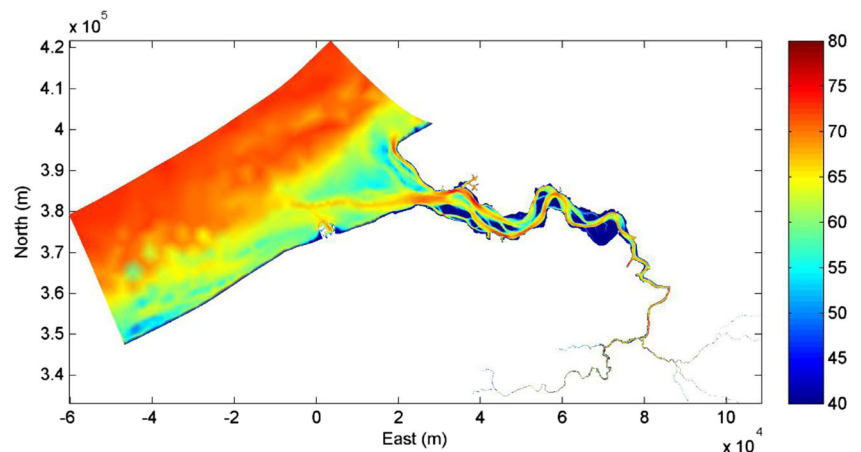
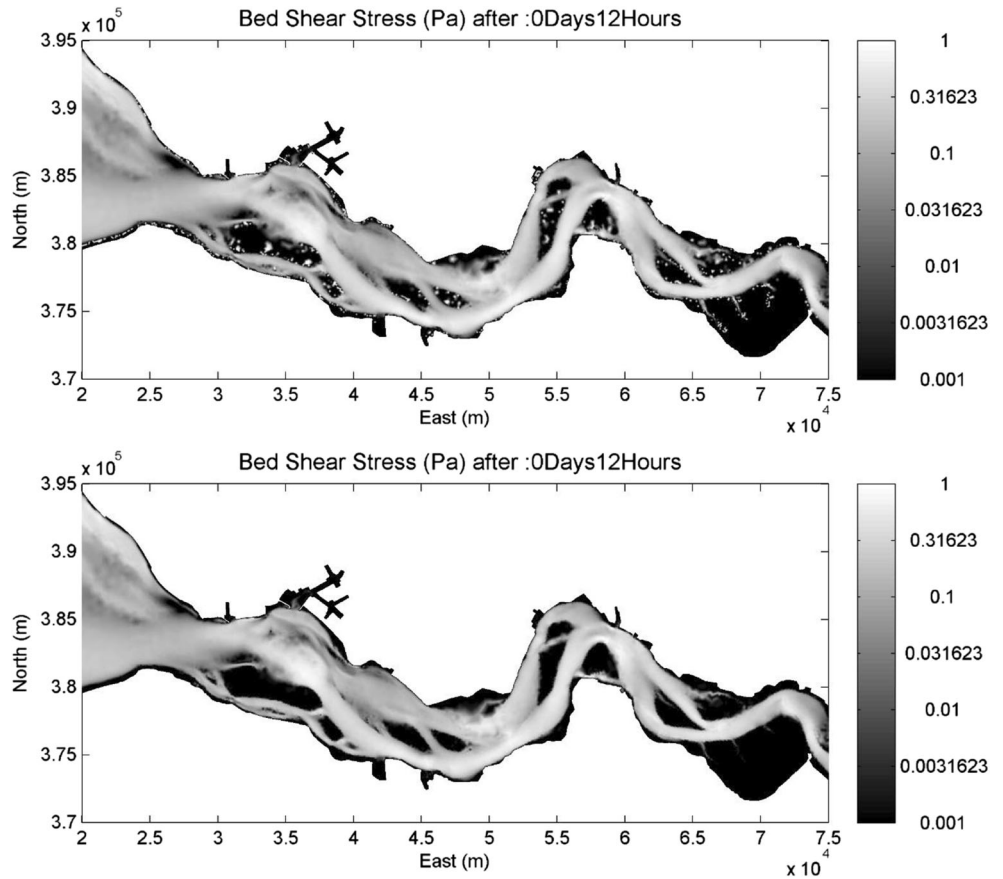


**Fig. 9** Comparison of bed shear stress in the central part of the Western Scheldt estuary for a traditional constant roughness parameter model (*top*) and the new friction law (*bottom*), in the case of a very small inundation threshold (1 mm). Without the improved roughness model, excessive erosion is predicted in the intertidal areas because of the incorrect prediction of the bed shear stress



Momentum along x:

$$\frac{\partial(hu)}{\partial t} + \frac{\partial(huu)}{\partial x} + \frac{\partial(huv)}{\partial y} = -gh\frac{\partial Z_s}{\partial x} + S_x + \nabla \cdot [h(\nu + \nu_t)\nabla u] \quad (2)$$

Momentum along y:

$$\frac{\partial(hv)}{\partial t} + \frac{\partial(huv)}{\partial x} + \frac{\partial(hvv)}{\partial y} = -gh\frac{\partial Z_s}{\partial y} + S_y + \nabla \cdot [h(\nu + \nu_t)\nabla v] \quad (3)$$

**Fig. 10** Measurement locations from MUMM

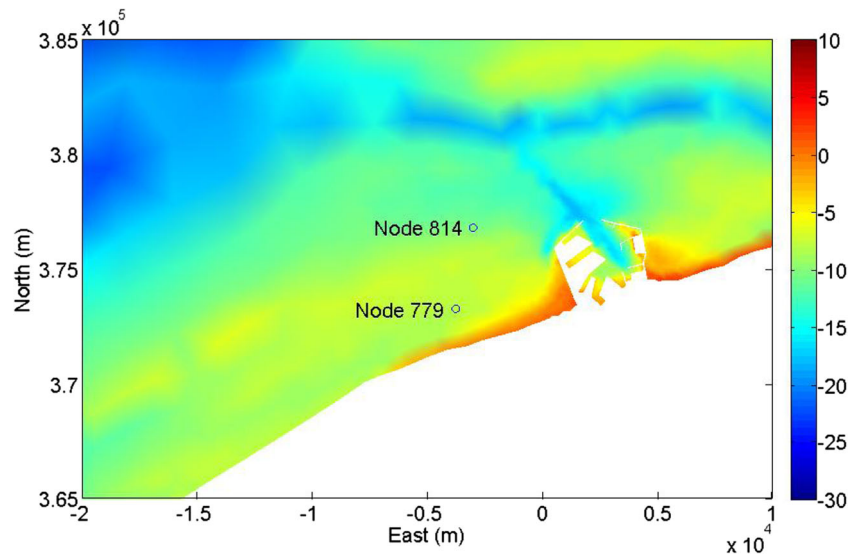


**Table 2** Measurement locations from MUMM

| Data Set                   | WGS coordinates               | Corresponding node in model | ADV measured at                      | OBS measured at                      |
|----------------------------|-------------------------------|-----------------------------|--------------------------------------|--------------------------------------|
| MOMO 2009-02-09–2009-03-19 | N 51° 21.490', E 003° 07.104' | 814                         | 0.36 m above bottom<br>(−7.38 m TAW) | 2.34 m above bottom<br>(−5.40 m TAW) |
| MOMO 2009-03-26–2009-04-29 | N 51° 21.474', E 003° 07.002' | 814                         | 0.36 m above bottom<br>(−7.38 m TAW) | 2.34 m above bottom<br>(−5.40 m TAW) |
| MOMO 2009-05-04–2009-06-15 | N 51° 19.572', E 003° 06.545' | 779                         | 0.38 m above bottom<br>(−4.87 m TAW) | 2.16 m above bottom<br>(−3.09 m TAW) |

Tracer conservation:

$$\frac{\partial(hT)}{\partial t} + \frac{\partial(hTu)}{\partial x} + \frac{\partial(hTv)}{\partial y} = S_T + \nabla \cdot (h\nu_T \nabla T) \quad (4)$$

in which  $h$ =water depth (m);  $u$  and  $v$ =velocity components (m/s);  $T$ =passive (non-buoyant) tracer;  $g$ =the gravity acceleration (m/s<sup>2</sup>);  $\nu_t$ =turbulent viscosity (m<sup>2</sup>/s) and  $\nu$ =kinematic water viscosity (m<sup>2</sup>/s);  $\nu_T$ =the tracer diffusivity coefficient;  $Z_s$ =free surface elevation (m);  $t$ =time (s);  $x$  and  $y$ =horizontal space coordinates (m);  $S_x$  and  $S_y$ =source terms representing the wind, Coriolis force, bottom friction, a source or a sink of momentum within the domain; and  $S_T$ =the tracer source or sink term.

For modelling the turbulent stress, a sub-grid turbulence model developed by Smagorinsky (1963) is adopted in this study. In principle, if the size of finite elements is small enough to allow the reproduction of all mechanisms including the viscous dissipation of very small vortices, turbulence would naturally appear in the solution of the Navier–Stokes equations. This requires the mesh size no

larger than the Kolmogorov microscales. The Smagorinsky model adds a turbulent viscosity deduced from a mixing-length model to the molecular viscosity, which compensates for the sub-grid-scale turbulent vortices which modelling is inhibited by the size of elements (Hervouet 2007). This method assumes that the energy production and dissipation of the small scales are in equilibrium. The Smagorinsky model can be summarised as:

$$\tau_{ij} - \frac{1}{3} \tau_{kk} \delta_{ij} = -2\rho C_s^2 \Delta^2 |\bar{S}| S_{ij} \quad (5)$$

$$\bar{S} = \sqrt{2S_{ij}S_{ij}} \quad (6)$$

The turbulent viscosity is modelled by

$$\nu_t = C_s^2 \Delta^2 \sqrt{2S_{ij}S_{ij}} \quad (7)$$

$$S_{ij} = \frac{1}{2} \left( \frac{\partial u_i}{\partial x_j} + \frac{\partial u_j}{\partial x_i} \right) \quad (8)$$

**Fig. 11** Measurement locations from Rijkswaterstaat, Centre for Water Management (The Netherlands)

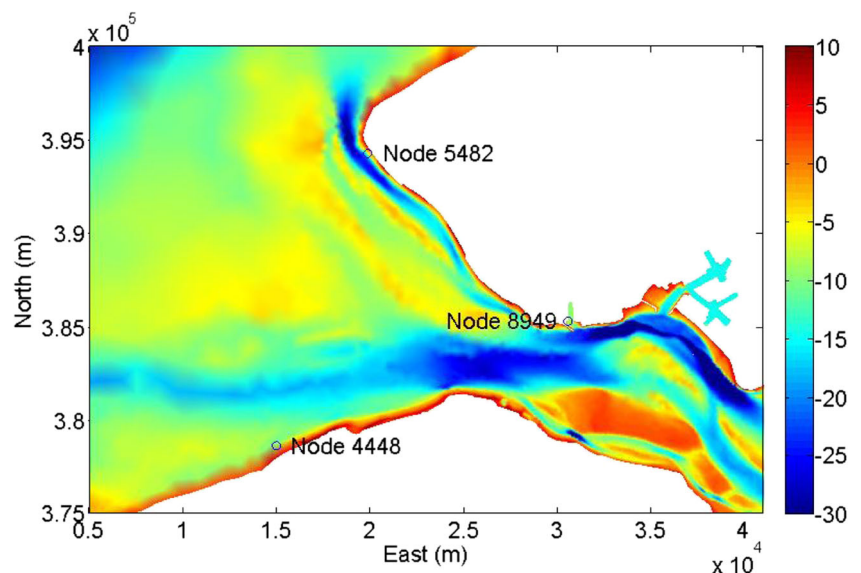


**Table 3** Measurement Locations from Rijkswaterstaat, Centre for Water Management, The Netherlands

| Data Set    | RD coordinates      | Corresponding node in the model |
|-------------|---------------------|---------------------------------|
| Cadzand     | 15004.07, 378597.07 | 4448                            |
| Vlissingen  | 30568.36, 385259.06 | 8949                            |
| Westkapelle | 19872.47, 394230.44 | 5482                            |

where  $\tau_{ij}$ =the Reynolds stress tensor ( $\text{kg}\cdot\text{m}^{-1}\cdot\text{s}^{-2}$ );  $\delta_{ij}$ =Kronecker delta;  $\rho$ =the water density ( $\text{kg}/\text{m}^3$ );  $C_s$ =the dimensionless coefficient, which ranges from 0.1 (channel flow) to 0.2 (isotropic turbulence);  $\Delta$ =the mesh size (m) derived in 2D from the surface of the elements; and  $S_{ij}$ =the strain rate tensor of average motion ( $\text{s}^{-1}$ ); the subscripts  $i$  and  $j$  are the indices of the Cartesian coordinates.

The model implementation focusses on the Scheldt estuary, which has been extended with a limited part of the Belgian coastal area, including necessary mesh refinements to model in detail the tide-affected docks of the Ports of Antwerp and Zeebrugge (Fig. 2). The bathymetry data is taken from the NEVLA model (Hartuiker 2004; van Kessel et al. 2011; Maximova et al. 2009b). It covers the whole Western Scheldt, starting from the upstream river and its tributaries in Belgium, extending all the way to the Belgian coast and the southwest coast of The Netherlands, including part of the North Sea. In 2009, a new survey was conducted and

**Table 4** Measurement locations from Flanders Hydraulics Research and IMDC

| Data Set            | RD coordinates      | Corresponding node in the model | Measured at                     |
|---------------------|---------------------|---------------------------------|---------------------------------|
| Prosperpolder       | 75037.24, 374074.43 | 27326                           | 2.5 m above bottom (-1.5 m TAW) |
| Boei84 (bottom)     | 77497.29, 370424.16 | 28492                           | 0.8 m above bottom (-8.1 m TAW) |
| Oosterweel (bottom) | 83903.55, 361552.10 | 30783                           | 1.0 m above bottom (-5.8 m TAW) |

subsequently the bathymetric data of the Western Scheldt was updated (Maximova et al. 2009a). The mesh used in the simulations is unstructured and non-uniform. It has 67,689 linear triangular elements and 37,527 nodes. In order to reduce the computational cost but maintain the accuracy as much as possible, a space varying resolution is adopted in the mesh. For the North Sea, the grid size is from 1000 to 2000 m because the bottom elevation does not change rapidly in this part of the domain and it is not necessary to have every detail in the North Sea. Approaching the coast, the mesh resolution becomes finer and finer. After entering the river mouth, the grid size is optimised in order to be better aligned along iso-depth lines. In certain areas, the grid size decreases to 50–100 m. This is due to the complex topography in those relatively shallow areas. There are many tidal flats in this region and the slopes often reach very high values, especially at those nodes close to the tidal flats and banks. Therefore, in such cases, a higher resolution could make the computation more stable. It is also necessary to provide sufficient detail when investigating the flow field and sedimentology in the estuary.

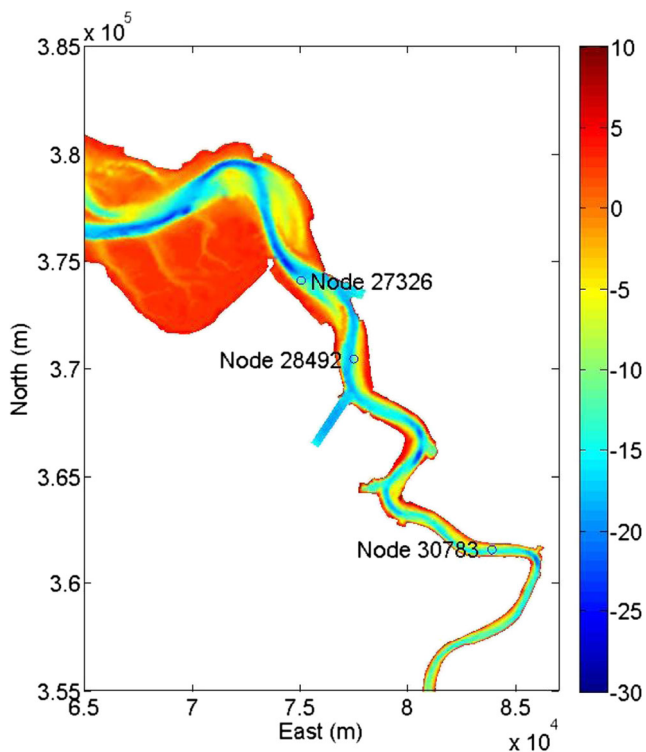


**Fig. 12** Measurement locations from Flanders Hydraulics Research and IMDC

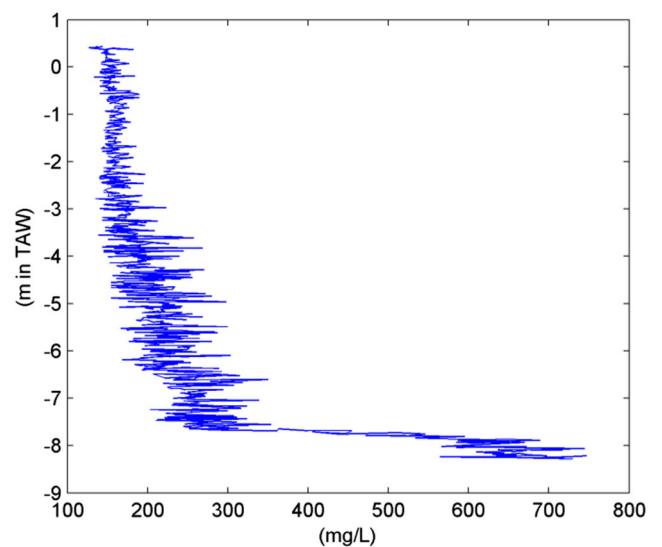
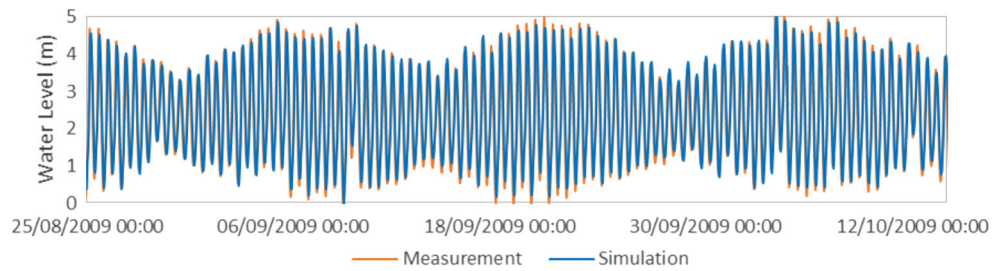


**Fig. 13** Typical suspension concentration profile measured at Deurganckdok at 16th February 2005. The calculated depth-averaged concentration at this particular location is 220.45 mg/l



**Fig. 14** Water level at node 4448



There are eight open (i.e. liquid) boundaries in the model, one downstream (the “sea boundary”) and seven upstream (one for each tributary). The rest are closed boundaries. All of the water boundaries have prescribed boundary conditions. The upstream boundaries are modelled as freshwater inflows. The annual-averaged river discharge of the Scheldt River near Schelle, at the confluence of the Rupel and the Scheldt, amounts to  $110 \text{ m}^3/\text{s}$  with approximately equal contributions from both tributaries (Kuijper et al. 2004). Therefore, in this study, a constant discharge is given to the upstream boundaries. The total amount of discharge is divided into two parts. The contribution from the three tributaries in the south-west is split evenly and accounts for half the amount of discharge to the mainstream. Similarly, the rest of the tributaries in the south-east contribute another half. Numerical tests confirm that the upstream inflow has little influence on the simulated results in the interested area since the upstream discharge is negligible compared with the inflow from the downstream boundary (the percentage of water flux passing through the upstream boundaries only ranges from 0.01 to 0.03 % compared to the amount from the sea boundary). The freshwater inflow normally has a salinity level of 0.5 ppt (Flanders Hydraulics Research, personal communication), and this has been assigned as the value for the salinity tracer as the upstream boundary condition. The downstream boundary includes part of the North Sea. The tidal elevation and salinity data are imposed at the downstream boundary. The nodes along the boundary have been adjusted to the same positions as those in the NEVLA model so that tidal elevation along the boundary nodes can be taken identical to the ones that drive the NEVLA model. The original data of tidal elevation along the boundary has a time interval of 10 min. Therefore, a numerical interpolation is performed in order to match the model time step (5 s). To obtain smooth transitions in the data, a

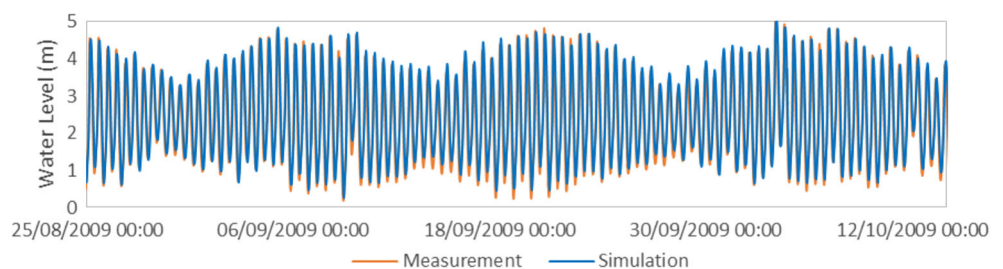
spline interpolation is used. This also enhances the model stability. At the downstream boundary, the salinity data from the NEVLA model are prescribed. The same spline interpolation is used to process the salinity data.

Dealing with tidal flats has always been a problematic part of hydrodynamics models. As seen in the bathymetric data, tidal flats are quite extensive all along the Scheldt Estuary, but especially in the lower estuary. Large amounts of saline, brackish or fresh water flow across these tidal flats within each tidal cycle. Thus, the tidal flats are constantly in transition between wet and dry conditions. Moreover, the slopes are usually quite steep around the tidal flats and may cause serious numerical problems if an inappropriate drying/flooding scheme is chosen. In the present model, all the finite elements are kept within the computational domain, which implies a specific treatment of dry points, especially when divisions by the depth occur in the equations. For example, the friction terms, as they appear in the non-conservative momentum equations, would become infinite on dry land, and are therefore limited in magnitude in the computation. Mass conservation is guaranteed with this option. Contrary to traditional models, the new friction law, presented in Section 2.3, ensures that the flow resistance becomes infinite when the water depth goes to zero. As demonstrated below, the present model does not require a threshold for the drying/flooding algorithm. This makes the model robust.

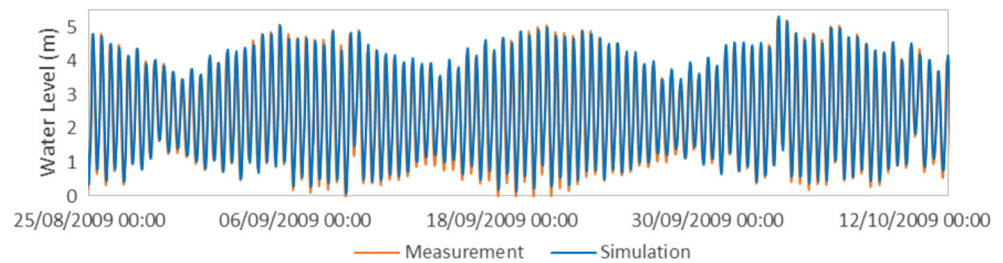
### 2.2 Sediment transport model

The sediment transport is modelled using SISYPHE, which is a sediment transport module inside OpenTELEMAC-MASCARET system. SISYPHE can be dynamically coupled with the TELEMAC-2D hydrodynamic model. At each time step, TELEMAC-2D exports the flow conditions to SISY

**Fig. 15** Water level at node 5482





**Fig. 16** Water level at node 8949

PHE, allowing it to compute the variables related to sediment transport, such as bedload and suspended concentration by mass (g/l). The bed evolution, i.e. the changes in bottom elevation, is sent back to TELEMAC-2D. The dynamic two-way coupling keeps the information in the separate modules up to date. When coupled, SISYPHE also shares the same boundary conditions with TELEMAC-2D. In order to fit the purpose of this study, the original code of SISYPHE has been customised.

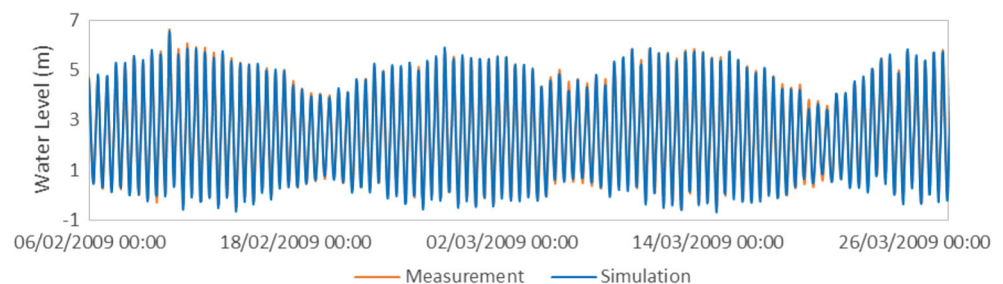
For the boundary conditions, there is no data set suitable for specifying the sediment flux at both upstream and downstream boundaries in the simulation period. For the non-cohesive sediment, the depth-averaged equilibrium concentration is calculated assuming equilibrium at the bed, and a Rouse profile correction is then applied. For the cohesive sediment, incoming sediment load is considered the same as the erosion flux at boundary nodes. No solid discharge is prescribed at open boundaries, but the sediments are allowed to move freely throughout the computational domain and through all its open boundaries. Compared to the large domain of the estuary, the background concentrations from incoming sediment loads at both upstream and downstream boundaries have limited influence to the coastal area and the main navigation channels in Scheldt. This confirms what has been known for years that most sediments recirculate within the Belgian coastal area (Malherbe 1991).

The bed composition in the Western Scheldt is dominated by sand, while in certain locations along the Belgian coast as well as far away in the upstream near the Port of Antwerp, high percentages of mud can be observed. Figure 3 shows the sand distribution map in the domain, which is used as initial bed composition in the model. Due to the lack of data in the

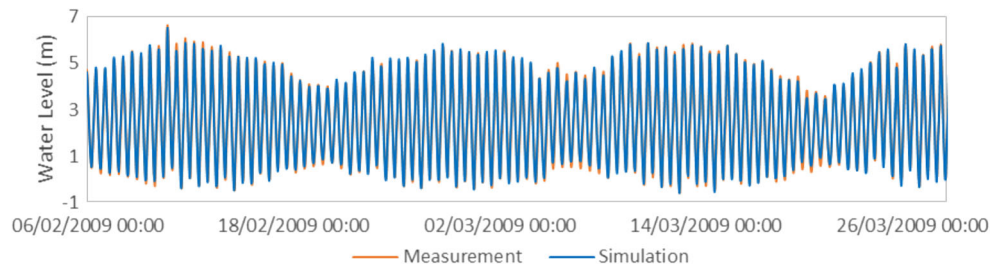
upstream river tributaries (upstream of Schelle), a default sand fraction is assigned to the bottom. The applied value was determined to be 90 %, which allows smooth transition from upstream to downstream.

The sediment bottom shows varying properties with depth as a result of alternating erosion and deposition events and of self-weight compaction (consolidation). In the top layer, sediment particles are usually freshly deposited to the bed. They are loosely packed, and a relatively low shear velocity can bring them back into the water column. The older layers underneath have had time to consolidate. The sediment volume has compacted, the density increased and the physical properties have changed since deposition due to the effective stress from the gravitational compaction. Therefore, the sediment particles in the lower layer(s) can be much more resistant to the flow and require more energy to be eroded. These insights are translated into a rather simple two-layer bed model: a first layer, which is easily erodible with a thickness of 0.5 m, and a second layer, which is much more difficult to erode and with a thickness of 1.5 m. Although this model is a rather simplistic approximation of the real situation, it contains some essential characteristics such as the limited availability of erodible sediment for resuspension from the bottom.

The current study considers two types of bed material, non-cohesive (sand) and cohesive (mud) sediment. The properties of bed material used in the model are given in Table 1. For each type of sediment, the transport mechanism is different. Sand is mainly transported as bedload, cohesive sediment mainly as suspended load, but both modes of transport consume energy. From this perspective, the available energy in the system is likely to be overestimated if only considering

**Fig. 17** Water level at node 27326

**Fig. 18** Water level at node 28492



cohesive or non-cohesive sediments. Thus, a new scheme accounting for mixed-sediment transport has been developed (Fig. 4).

The bedload is calculated only for non-cohesive sediment. The formula from van Rijn (1984) is used:

$$q^* = \frac{0.053}{d^{*0.3}} \left( \frac{\tau^*}{\tau_{crit}^*} - 1 \right)^{2.1} \tag{9}$$

and:

$$q^* = \frac{q_b}{\sqrt{(s-1)gd^3}} \tag{10}$$

$$\tau^* = \frac{\tau_b}{\rho(s-1)gd} \tag{11}$$

$$d^* = d \left[ \frac{(s-1)g}{\nu^2} \right]^{1/3} \tag{12}$$

in which  $q^*$ =dimensionless bed flux,  $\tau^*$ =Shields stress,  $d^*$ =dimensionless particle diameter,  $q_b$ =bedload transport rate ( $m^2/s$ ) (volume rate of transport per unit length of surface),  $\tau_b$ =bed shear stress ( $kg\ m^{-1}\ s^{-2}$ ),  $d$ =particle diameter (m),  $\rho_s$ =sand density ( $kg/m^3$ ),  $\rho$ =fluid density ( $kg/m^3$ ),  $s=\rho_s/\rho$

relative density,  $\nu$ =kinematic viscosity of fluid ( $m^2/s$ ) and  $g$ =gravity acceleration ( $m/s^2$ ).

Suspended-load concentration in a depth-averaged model is obtained by integrating the 3D sediment transport equation over the water depth:

$$\frac{\partial hC}{\partial t} + \frac{\partial(hUC)}{\partial x} + \frac{\partial(hVC)}{\partial y} = \frac{\partial}{\partial x} \left( h\epsilon_s \frac{\partial C}{\partial x} \right) + \frac{\partial}{\partial y} \left( h\epsilon_s \frac{\partial C}{\partial y} \right) + E - D \tag{13}$$

where  $C$ =the total suspension concentration ( $kg/m^3$ );  $h$ =water depth (m) (assuming that the bedload layer thickness is very thin);  $U$  and  $V$ =the depth-averaged velocity components ( $m/s$ );  $\epsilon_s$ =the diffusion coefficient,  $E$ =erosion flux ( $kg\ m^{-2}\ s^{-1}$ ); and  $D$ =deposition flux ( $kg\ m^{-2}\ s^{-1}$ ).

In the Scheldt estuary, the effective settling velocity can be affected by many factors, e.g. initial suspension concentration, flow unsteadiness, waves and tidal phase effects, which may cause a delayed settling of sediment particles (da Silva et al. 2006). For the cohesive sediment, the commonly used settling velocity in the Scheldt estuary is about 0.001 m/s, which is generally larger than the settling velocity based on the individual particle size; thus, it implicitly accounts for the aggregation of cohesive particles into flocs (Fettweis and Van den Eynde 2003; van Kessel et al. 2011; Dam and Blik 2013). The settling velocity of sand in the Scheldt estuary is set to 0.01 m/s, following the study of Hoogduin et al. (2009). Dam et al. (2007) used a slightly higher value 0.015 cm/s as the fall velocity of sand in their morphological model of the Western Scheldt estuary. The sedimentation and erosion patterns and

**Fig. 19** Water level at node 30783

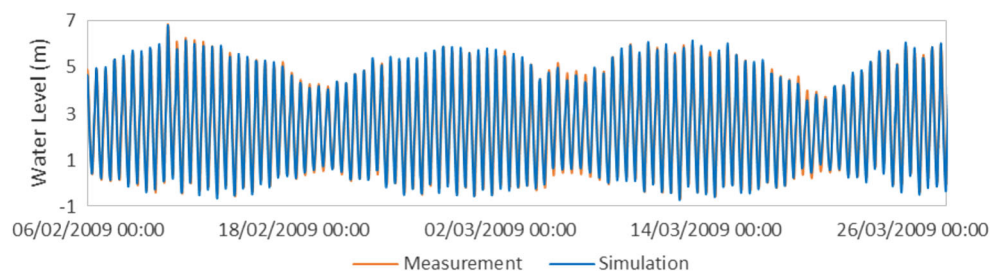
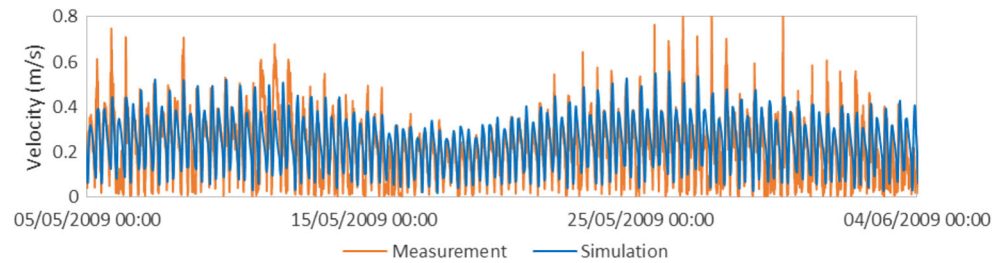


**Fig. 20** Velocity magnitude at node 779



magnitude reproduced by the model close to the Port of Zeebrugge is consistent with the observations from the Quest4D project (Figs. 32 and 33), which also supports that the settling velocity for this study is appropriate. However, one should realise that the latter value also compensates for the fact that resuspension by waves, which is known to play an important role in the coastal zone, is not accounted for in the present model.

Fettweis and Van den Eynde (2003) suggest that the bulk density of mud found near Zeebrugge is about  $1500\text{--}1600\text{ kg/m}^3$ , and the critical shear stress for erosion varies between 0.5 Pa (freshly deposited mud) and 0.8 Pa (after 48 h). Due to the existence of two types of sediment particles, the critical shear stress for erosion of a mixture is the combination of the values of sand and mud. The commonly used values for pure sand (0.2–0.35 Pa) cannot represent the mixture properties and lead to excessive erosion of the fine fraction. Therefore, the numerical tests suggest a higher value for the critical shear stress for erosion. The most significant effect on erosion resistance occurs on the addition of small percentages by weight of mud to sand. This is confirmed by the study of Mitchener and Torfs (1996), in which the critical shear stress for erosion can be easily above 0.5 Pa with just a small fraction (4–5 %) of cohesive mud added in. Because the bed composition data shows that a fraction of mud is observed almost everywhere in the domain, the higher value of critical shear stress for erosion of sand is considered as appropriate in this study.

During the erosion phase, the methodology for modelling mixed-sediment from Waeles (2005) is employed. According to his study, the sand–mud mixture can be categorised as non-cohesive, mixed and cohesive, based on its sand–mud composition. Each category has its unique

characteristics and behaviour. For the application in the Scheldt Estuary, the lower bound of the critical mud fraction is set to 30 % and the upper bound is 50 %. The mixture that contains mud <30 % is in the non-cohesive regime and is considered as sand; those having mud >50 % are in the cohesive regime and are treated as mud; the rest is in the mixed-sediment regime. The lower and upper bounds of critical mud fractions is suggested by the study of Panagiotopoulos et al. (1997) and Mitchener and Torfs (1996). As the mud fraction increases, the available space between the sand grains decreases. When the mass fraction of mud is lower than about 30 % (corresponding to volume fraction approximately 11 %), the sand grains remain in contact with each other. When the mud fraction exceeds 30 %, spaces between sand particles are filled by mud particles, which can form a matrix, and, in this case, pivoting is no longer the main mechanism responsible for resuspension of sand grains. Consequently, the whole mixture does not behave like a non-cohesive sediment any more. In Mitchener and Torfs' study, the critical shear increases significantly when mud is added to sand (0–30 % mud). There is an optimal ratio of sand content in a mixed bed at which the critical erosion shear stress is a maximum. The optimum sand fraction appears to be between 50 and 70 % by weight of sand. Therefore, the lower and upper bounds of critical mud fractions were set at 30 and 50 %. These values are also used in the study of Waeles et al. (2007). The critical shear stress for erosion is calculated as function of the mud fraction ( $f_m$ ) as follows (Waeles 2005):

Non-cohesive regime ( $f_m < 30\%$ ):

$$\tau_{ce} = \tau_{ce,s} + x_1 \cdot f_m \quad (14)$$

**Fig. 21** Velocity magnitude at node 814

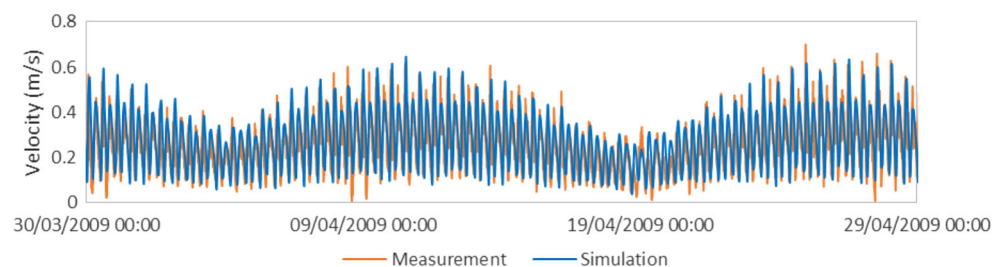
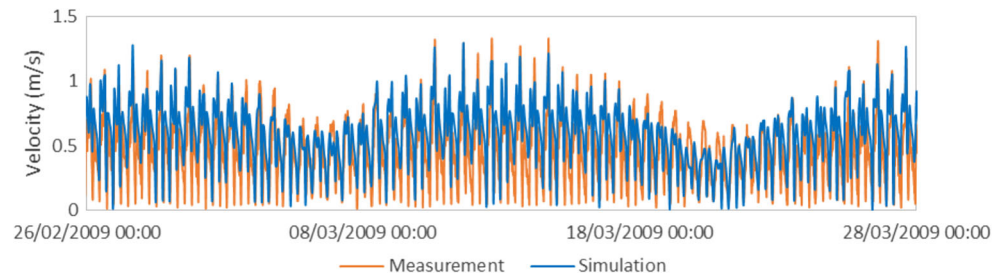


**Fig. 22** Velocity magnitude at node 28492



Mixture regime ( $30 \% < f_m < 50 \%$ ):

$$\tau_{ce} = \frac{\tau_{ce,s} + x_1 \cdot f_{m,crit}}{f_{m,crit*} - f_{m,crit}} (f_{m,crit*} - f_m) + \frac{f_m - f_{m,crit}}{f_{m,crit*} - f_{m,crit}} \tau_{ce,m} \tag{15}$$

Cohesive regime ( $f_m > 50 \%$ ):

$$\tau_{ce} = \tau_{ce,m} \tag{16}$$

where  $\tau_{ce}$ ,  $\tau_{ce,s}$  and  $\tau_{ce,m}$  = the critical shear stresses ( $\text{kg m}^{-1} \text{s}^{-2}$ ) for erosion of mixture, sand and mud respectively;  $x_1$  = a calibration constant; and  $f_{m,crit}$  and  $f_{m,crit*}$  = the lower and upper bounds of critical mud fraction, respectively.

The calibration constant  $x_1$  is 0.5 in the current study, which is considered suitable for the Scheldt estuary according to the studies of Mitchener and Torfs (1996) and Fettweis and Van den Eynde (2003). Figure 5 shows the critical shear stress for erosion as a function of the mud fraction in two bed layers. In the non-cohesive regime, sediment particles behave like sand, so the consolidation process is ignored. The critical shear stress for erosion increases when the mud is added to sand. When the mud fraction exceeds 30 %, the transitional regime is reached where different behaviour in the upper and lower bed layers is expected. In the upper layer, the excessive mud particles will accumulate and due to the loose form,

the critical shear stress for erosion begins to decrease; in the lower layer, the consolidation process will give extra erosion resistance to the bed material. When the mud fraction exceeds 50 %, the maximum critical shear stress for erosion is reached in the lower layer, which is 0.8 Pa, the same as for mud consolidated for over 48 h; while in the upper layer, the sediment behaves like freshly deposited mud, so the same value of 0.5 Pa is assigned. The calibration constant  $x_1$  is set to 0.5 to ensure the critical shear stress for erosion does not exceed the maximum value before the mud fraction exceeding 50 %, to preserve the characteristics of the sand–mud mixtures in different regimes.

The erosion rate can be determined depending on the regime of the mixed sediment following the same procedure of Waeles (2005):

Non-cohesive regime ( $f_m < 30 \%$ ):

$$E_s = (1 - f_m) \cdot E_{0s} \cdot T^a \tag{17}$$

$$E_m = f_m \cdot E_{0s} \cdot T^a \tag{18}$$

Mixture regime ( $30 \% < f_m < 50 \%$ ):

$$E_s = (1 - f_m) \cdot \left[ E_{0s} + \frac{E_{0m} - E_{0s}}{f_{m,crit*} - f_{m,crit}} (f_m - f_{m,crit}) \right] \cdot T \left[ a + \frac{1-a}{f_{m,crit*} - f_{m,crit}} (f_m - f_{m,crit}) \right] \tag{19}$$

**Fig. 23** Velocity magnitude at node 30783

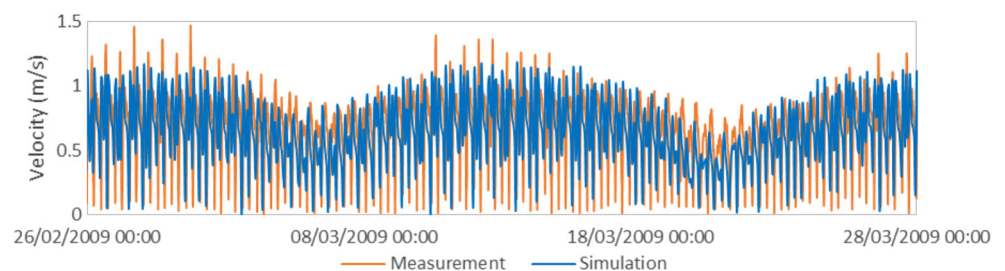
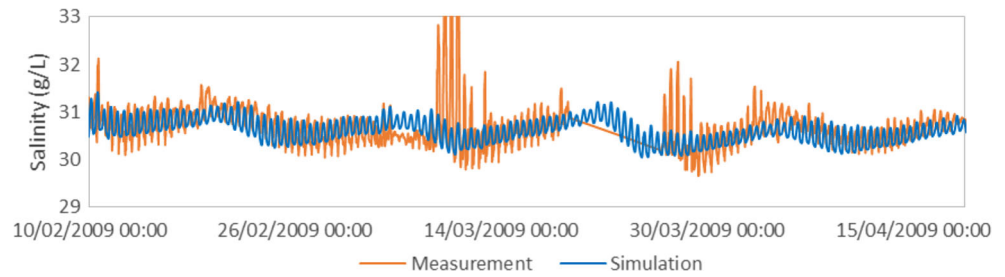




**Fig. 24** Salinity at node 814



$$E_m = f_m \cdot \left[ E_{0s} + \frac{E_{0m} - E_{0s}}{f_{m,crit} - f_{m,crit}} (f_m - f_{m,crit}) \right] \cdot T \left[ a + \frac{1-a}{f_{m,crit} - f_{m,crit}} (f_m - f_{m,crit}) \right] \quad (20)$$

Cohesive regime ( $f_m > 50\%$ ):

$$E_s = (1 - f_m) \cdot E_{0m} \cdot T \quad (21)$$

$$E_m = f_m \cdot E_{0m} \cdot T \quad (22)$$

in which  $E_s$  and  $E_m$  = the erosion rate ( $\text{kg m}^{-2} \text{s}^{-1}$ ) for sand and mud, respectively;  $E_{0s}$  and  $E_{0m}$  = the erosion constant ( $\text{kg m}^{-2} \text{s}^{-1}$ ) for non-cohesive regime and cohesive regime, respectively;  $T = (\tau - \tau_{ce}) / \tau_{ce}$ ,  $\tau$  = the bed shear stress ( $\text{kg m}^{-1} \text{s}^{-2}$ );  $\tau_{ce}$  = the critical shear stress ( $\text{kg m}^{-1} \text{s}^{-2}$ ) for erosion; and  $a = 0.5$ , a constant suggested in the study of Waeles et al. (2007), which is suitable for most cases.

The erosion constants  $E_{0s}$  and  $E_{0m}$  are determined based on the study of Mitchener and Torfs (1996), in which they reported that the erosion rate for pure mud beds ( $0.05\text{--}0.1 \times 10^{-3} \text{ kg m}^{-2} \text{ s}^{-1}$ ) was an order of magnitude higher than for the 20 and 40 % sand beds ( $0.005\text{--}0.03 \times 10^{-3} \text{ kg m}^{-2} \text{ s}^{-1}$ ). Therefore, in this study, the erosion constant  $E_{0s}$  for the non-cohesive regime is assumed  $0.01 \times 10^{-3} \text{ kg m}^{-2} \text{ s}^{-1}$ , and the erosion constant  $E_{0m}$  for the cohesive regime is  $0.1 \times 10^{-3} \text{ kg m}^{-2} \text{ s}^{-1}$ .

Since the vertical energy balance is not resolved in a 2DH model, the traditional deposition law, proposed by

Krone (1962), is used. A new deposition criterion, which has been derived from a suspension capacity condition proposed by Toorman (2000 and 2002), has been introduced in this study, which allows estimating the critical stress for deposition in each node and no longer needs calibration. Since shear flow produces turbulence, the critical ‘shear stress’ for deposition can be related to the total amount of turbulent energy that is required to keep a number of sediment particles in suspension. When the bed shear stress cannot provide the fluid with enough energy that is needed to maintain all the suspended particles in the water column, deposition shall begin. The excessive sediment settles down to the bottom until the energy balance is restored.

The critical shear stress for deposition, obtained by inversion of Toorman’s suspension capacity criterion, has been split into two parts in order to deal with sand–mud mixtures. In this case, the total required turbulent energy is also divided over both sediment fractions: Part of it is used to keep non-cohesive particles in suspension, and the rest is used to keep cohesive particles in suspension. The corresponding ‘critical stresses’ are given in the following equations:

$$\tau_{cd,s} = \frac{(1 - \rho_w / \rho_s)gh}{Rf} \frac{w_s C_s}{U} \quad (23)$$

$$\tau_{cd,m} = \frac{(1 - \rho_w / \rho_m)gh}{Rf} \frac{w_m C_m}{U} \quad (24)$$

**Fig. 25** Salinity at node 27326

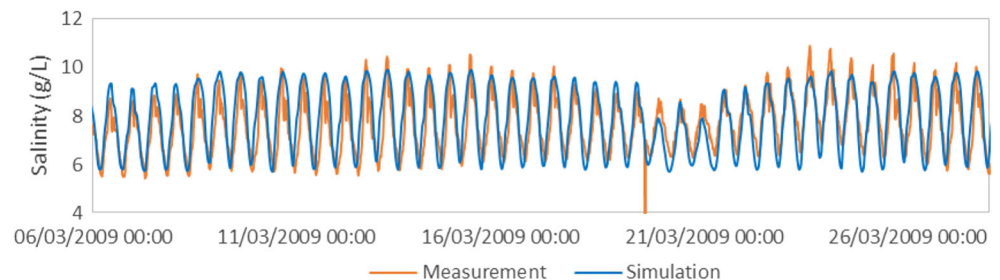
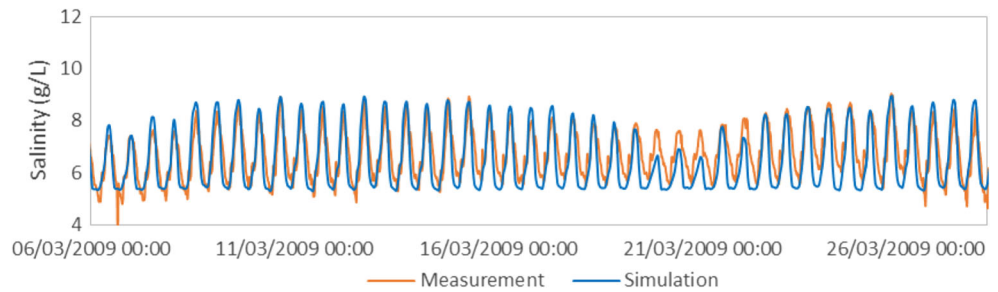




**Fig. 26** Salinity at node 28492



$$Rf = 0.25 \left( \frac{u_*}{w_a} \right)^2 \cdot \frac{0.01}{1 + 0.01 \left( \frac{u_*}{w_a} \right)^2} \quad (25)$$

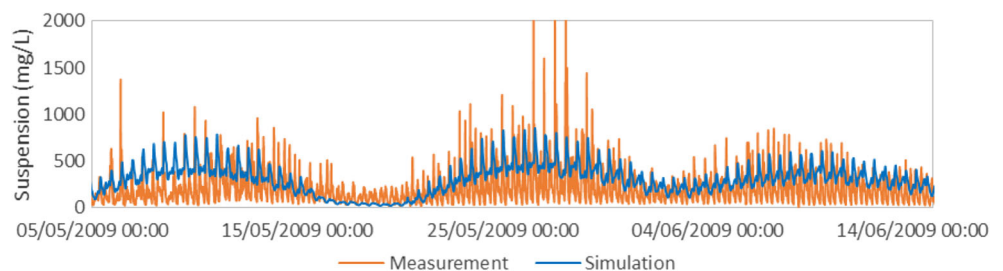
$$w_a = \frac{w_s C_s + w_m C_m}{C_s + C_m} \quad (26)$$

where  $\tau_{cd,s}$  and  $\tau_{cd,m}$  = the critical shear stress ( $\text{kg m}^{-1} \text{s}^{-2}$ ) for sand and mud deposition, respectively;  $\rho_w$  is the fluid density ( $\text{kg/m}^3$ );  $\rho_s$  = sand density ( $\text{kg/m}^3$ );  $\rho_m$  = mud density ( $\text{kg/m}^3$ );  $Rf$  = flux Richardson number for mixture at suspension capacity, which expresses the ratio of suspension potential to turbulent kinetic energy (its value is usually  $< 0.1$ , based on the analysis of various experimental data sets from field and laboratory measurements; Toorman 2003);  $u_*$  = the shear velocity (m/s);  $g$  = gravity acceleration ( $\text{m/s}^2$ );  $w_s$  and  $w_m$  = the settling velocities (m/s) of sand and mud, respectively;  $w_a$  = the averaged settling velocity (m/s) of mixture;  $C_s$  and  $C_m$  = the depth-averaged suspension mass concentration ( $\text{kg/m}^3$ ) of sand and mud, respectively; and  $U$  = the magnitude of velocity (m/s).

Krone's deposition law (1962) subsequently is adapted to be used for calculating the deposition flux of each fraction, without violating the energy balance:

$$p_s = \max \left[ 1 - \frac{C_s}{C_s + C_m} \frac{\tau}{\tau_{cd,s}}, 0 \right] \quad (27)$$

**Fig. 27** Suspended-sediment concentration at node 779



$$p_m = \max \left[ 1 - \frac{C_m}{C_s + C_m} \frac{\tau}{\tau_{cd,m}}, 0 \right] \quad (28)$$

$$D_s = (w_s C_s) \cdot p_s \quad (29)$$

$$D_m = (w_m C_m) \cdot p_m \quad (30)$$

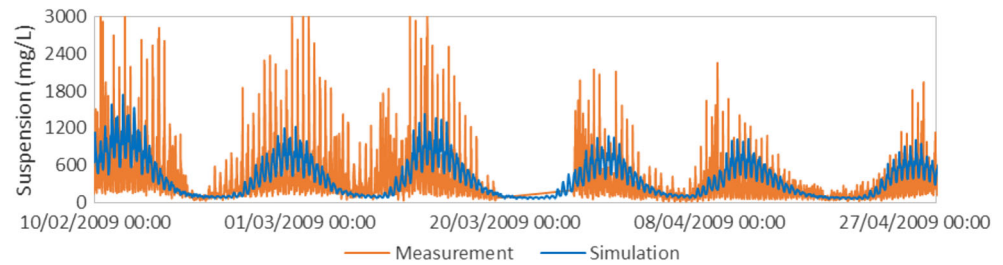
where  $p_s$  and  $p_m$  are deposition probabilities of sand and mud, respectively;  $D_s$  is the deposition flux ( $\text{kg m}^{-2} \text{s}^{-1}$ ) of sand; and  $D_m$  is the deposition flux of mud ( $\text{kg m}^{-2} \text{s}^{-1}$ ).

The bed evolution is calculated using the Exner equation with an additional source term, allowing the inclusion of external changes caused by the erosion and deposition of sediment particles. The following form of the Exner equation is used in the study:

$$(1-n) \frac{\partial Z_b}{\partial t} + \nabla \cdot Q_b + (E-D) = 0 \quad (31)$$

where  $n$  is the bed porosity,  $Z_b$  is the bottom elevation (m),  $Q_b$  is the bedload transport rate per unit width ( $\text{m}^2/\text{s}$ ),  $E$  is the erosion flux and  $D$  is the deposition flux (m/s). It is worth pointing out here that the bed porosity is an estimate value considering cohesive particles filling up part of the spaces

**Fig. 28** Suspended-sediment concentration at node 814



between non-cohesive particles, and the erosion and deposition flux consists of contributions from both cohesive and non-cohesive sediments.

When computing the bed evolution, an iterative procedure is employed, where at each time step, the top layer is eroded first. Once it is empty, the erosion of the second layer starts. The deposited sediment always has the properties of a fresh deposit, i.e. the critical shear stress is as in the first layer. The sand/mud composition, however, is recalculated at each time step based on the mass fraction of sand/mud at each particular location after erosion/deposition processes, and the latest value is assigned to the new deposits. The scheme is illustrated in Fig. 6.

### 2.3 The new friction law based on the generalised mixing-length theory

Part of the energy from currents and waves is dissipated by friction with the bottom and becomes more and more important with decreasing water depth. In theoretical and numerical models to quantify water and/or sediment movement, this energy loss is described by an empirical or semi-empirical roughness closure (van Rijn 1993). In practice, it introduces a single roughness parameter (sometimes related to the grain size of the bottom sediment or to bed form dimensions), which is calibrated by comparison of predicted and measured water levels.

Research, supported by laboratory and numerical experiments, has demonstrated that, in the presence of suspended sediments, the traditional approach is not able to predict the correct velocity fields, especially near the bottom (Toorman and Bi 2013a). This has serious implications for flows over shallow areas (i.e. near-shore and intertidal areas) and for the estimation of sediment budgets in particular. Therefore, hydrodynamic models for coastal and estuarine areas, in particular when applied to the nearshore and intertidal areas, should

be improved by implementation of a more physically based bottom-friction model.

For this purpose, a new modelling strategy developed by Toorman and Bi (2011, 2012, 2013a, b, c) has been implemented in the model for analysing the Western Scheldt estuary. It consists of a new generic friction model that accounts not only for the energy dissipation caused by the flow over the bottom roughness structures but also for the dissipation induced by the inertia of the suspended particles (Toorman 2011). The latter is no longer negligible above the bed where high concentrations of suspended matter are encountered. This process explains the drag modulation by suspended matter reported in the literature (Toorman and Bi 2013b, and references therein).

The new generic friction model is based on a GML theory, proposed by Toorman (in preparation) and inspired by the idea of van Driest (1956). By extending the validity of a turbulence model into the low-Reynolds layer, where viscous dissipation (and possibly other dissipation mechanisms) can no longer be neglected, down to the wall with a carefully calibrated damping function  $f_A$ , and accounting for the viscous stress in the laminar wall layer, the GML theory allows transient conditions being included in the model. In the case of a rough bottom, the introducing of a sub-grid-scale viscosity can account for the additional sub-grid-scale energy dissipation in the eddies generated between roughness elements. Similarly, turbulence generation in the wake of sediment particles, as already suggested by Elghobashi (1994), can also be taken into account.

The steady-state vertical stress balance at a distance  $z$  above the bed in open-channel flow of sediment-laden water can be written as:

$$\rho(\nu + \nu_{\text{SGS}} + \nu_t) \frac{\partial U}{\partial z} = \tau_0(1-\eta) \quad (32)$$

**Fig. 29** Suspended-sediment concentration at node 27326

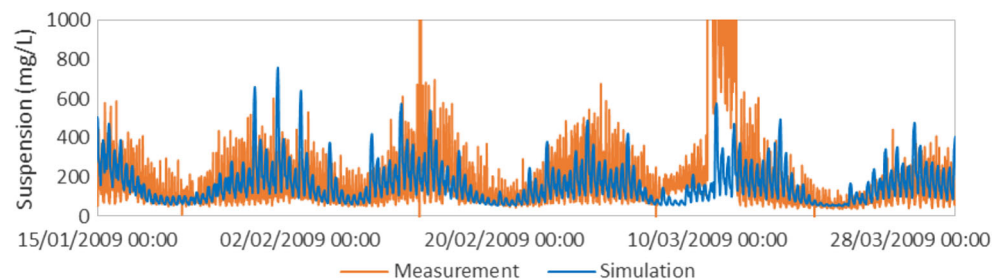
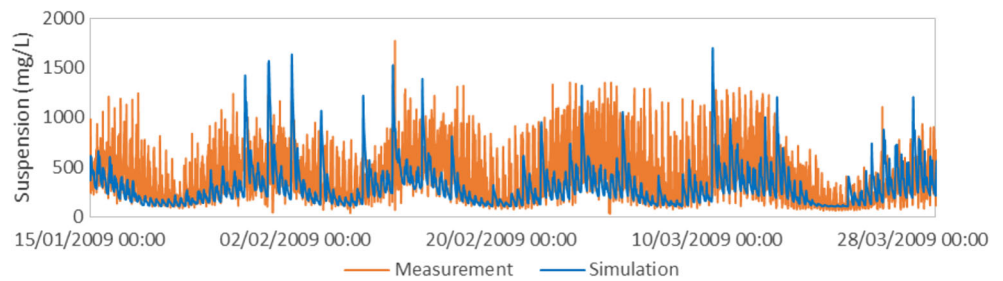


**Fig. 30** Suspended-sediment concentration at node 28492



where  $U$ =local flow velocity (m/s);  $\tau_0=\rho u_*^2$ =bed shear stress ( $\text{kg m}^{-1} \text{s}^{-2}$ ) with  $u_*$  the shear velocity (m/s);  $\eta=z/h$ , with  $h$ =water depth (m);  $\rho$ =density of the sediment-laden water ( $\text{kg/m}^3$ );  $\nu$ =kinematic viscosity of the sediment-laden water ( $\text{m}^2/\text{s}$ ) (including concentration effects, such as intergranular friction);  $\nu_t$ =turbulent eddy viscosity ( $\text{m}^2/\text{s}$ ); and  $\nu_{\text{SGS}}$ =sub-grid-scale turbulence ( $\text{m}^2/\text{s}$ ) generated by vortex shedding in the wake of bed roughness elements and/or of suspended particles. The eddy viscosity in the fully developed outer layer is computed with the well-known parabolic profile, following Prandtl’s mixing length theory (Prandtl 1925) applied to steady open-channel flow (Eq. 32 with neglect of  $\nu$  and  $\nu_{\text{SGS}}$ ). In the inner layer, comprising the intermediate transient layer and the viscous sublayer at the bottom, this eddy viscosity has to be corrected with an empirically determined damping function ( $f_A$ ).

Rearrangement and non-dimensionalisation of Eq. 32 yields:

$$\frac{\partial U_+}{\partial z_+} = \frac{(1-\eta)}{1 + B_+ + f_A \kappa z_+ (1-\eta)} \quad (33)$$

in which  $U_+=U/u_*$ =velocity  $U$  non-dimensionalised by the shear velocity  $u_*$ ;  $z_+=z u_*/\nu$ =distance from the bottom  $z$  non-dimensionalised by the length-scale  $\nu/u_*$ ;  $B_+=\nu_{\text{SGS}}/\nu$ =GML model parameter, empirically found to be proportional to the sediment concentration (cf. Fig. 7); and  $\kappa$ =the von Karman coefficient (which may have a lower value than the original constant 0.41 due to sediments in suspension). This new GML model has been calibrated against large eddy simulation (LES) data for open-channel flow over a wavy bottom from Widera

et al. (2009) and the experimental flume data for sand suspensions from Cellino (1998) (Fig. 7).

For engineering applications, the above theory has been converted into a 2DH friction model. In principle, this is obtained by computing the depth-averaged velocity by integration over depth of the theoretical velocity profile and solving the equation for the shear velocity  $u_*$ . In order to allow both transient conditions (i.e.  $5 < h_+ < 100$ —see Eq. 38) and the transition during drying/wetting of tidal flats, it is necessary to combine the laminar and turbulent contributions. However, since Eq. 33 does not allow an analytical solution, the procedure is applied to the theoretical parabolic profile for laminar flow and the logarithmic profile for fully developed turbulent flow (integrated from the roughness height to the surface). The final bed shear stress is then obtained by superposition of the laminar and the turbulent stress, applying a damping function to the turbulent stress towards the bottom (confirm observations, and simultaneously avoiding numerical problems). Therefore, the bed shear stress can be directly computed as follows (Toorman and Bi 2012):

$$\begin{aligned} \tau_b/\rho = u_*^2 = f_A u_{* \text{turb}}^2 + u_{* \text{lam}}^2 = f_A \left[ \frac{\kappa U}{\ln(h/z_0)-1 + z_0/h} \right]^2 \\ + \left[ \sqrt{\left( \frac{3}{2} (z_0 + \beta \varphi h) \frac{U}{h} \right)^2 + 3 \frac{U}{h} \nu(\varphi) + \frac{3}{2} (z_0 + \beta \varphi h) \frac{U}{h}} \right]^2 \end{aligned} \quad (34)$$

where  $\tau_b$ =the bed shear stress ( $\text{kg m}^{-1} \text{s}^{-2}$ );  $\rho$ =the density of water ( $\text{kg/m}^3$ );  $u_*$ =the shear velocity (m/s);  $u_{* \text{turb}}$ =the shear velocity for fully developed turbulent open-channel flow (m/s);  $u_{* \text{lam}}$ =the shear velocity for laminar open-channel flow

**Fig. 31** Suspended-sediment concentration at node 30783

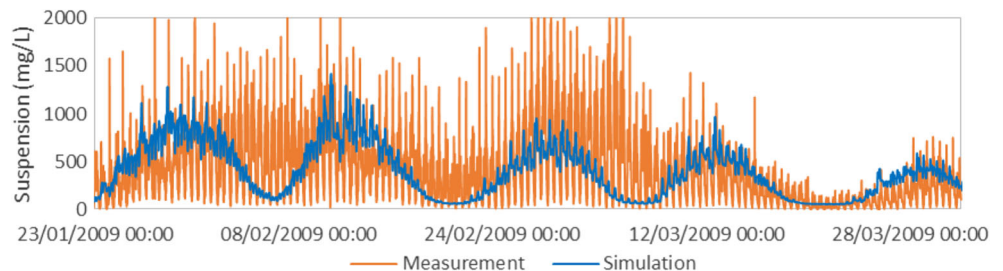
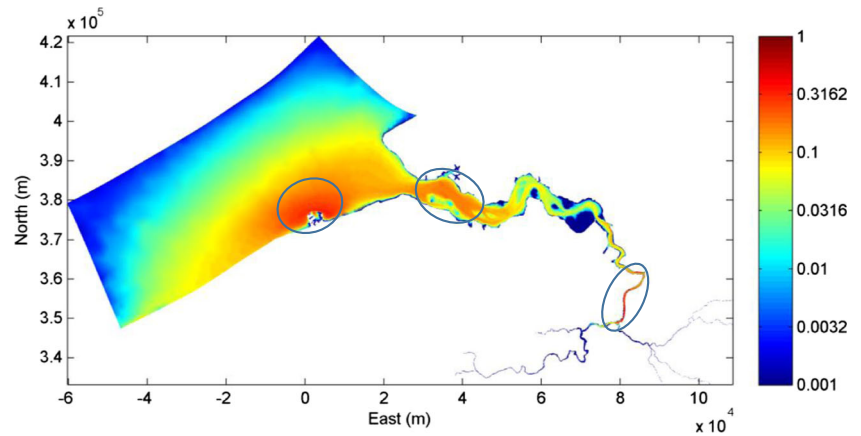


**Fig. 32** Suspension concentration (g/l) averaged over one tidal cycle on 4th December 2009



(m/s);  $\kappa$ =the von Karman coefficient (which decreases from the clear water value 0.41 to lower values depending on the sediment load);  $U$ =the local depth-averaged flow velocity (m/s);  $h$ =the local water depth (m);  $\beta$ =the suspension friction (or apparent roughness) coefficient, which is 0.045 (found using data fitting for Fig. 7);  $\nu_w$ =the water viscosity (m<sup>2</sup>/s);  $\varphi$ =the volumetric suspended particle concentration; and  $z_0$ =the effective roughness length scale (m).

Unlike other models, which assume hydraulic rough conditions,  $z_0$  is computed from the following relation, which covers the entire range from hydraulic smooth (first term on the right) to hydraulic rough (second term):

$$z_{0+} = \frac{z_0 u_*}{\nu} = \exp(-\kappa B_0) + f_\beta(k_{s+}) k_{s+} \exp(-\kappa B_\infty) \quad (35)$$

where  $z_0$  and  $k_s$  (the equivalent Nikuradse roughness length scale) are non-dimensionalised with  $\nu/u_*$  to  $z_{0+}$  and  $k_{s+}$ ;  $B_0=5.5$  and  $B_\infty=8.5$ , respectively, the smooth and rough values of the constant in the non-dimensional logarithmic velocity

profiles ( $u/u_* = \kappa^{-1} \ln(z/k_s) + B$ ) (Nikuradse 1933), and with an empirical damping function:

$$f_\beta(k_{s+}) = 1 - \exp[-k_{s+} \exp(-\kappa B_\infty)] \quad (36)$$

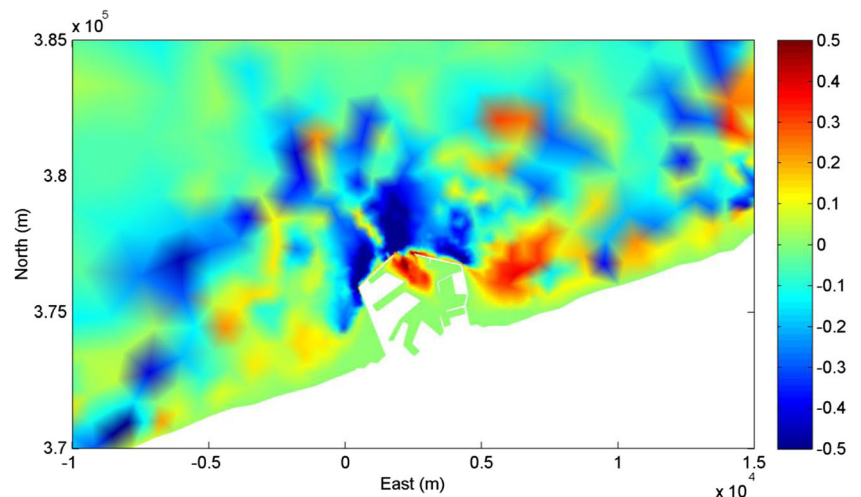
which matches the entire Nikuradse (1933) data set. In the present simulation,  $k_s=0.03$  m, considering bedforms. Extension to hydraulic smooth conditions is necessary to include the physics of transition to laminar thin film flow when the water depth goes to zero.

The turbulence damping factor  $f_A$  has the following form (similar to the damping function in Eq. 33):

$$f_A = [1 - \exp(-h_+/A_+)]^2 \quad (37)$$

with  $A_+=17$ , an empirical value, and with the water depth non-dimensionalised as:

**Fig. 33** Modelled erosion and accumulation (m) of sediment around Port of Zeebrugge after 1 year





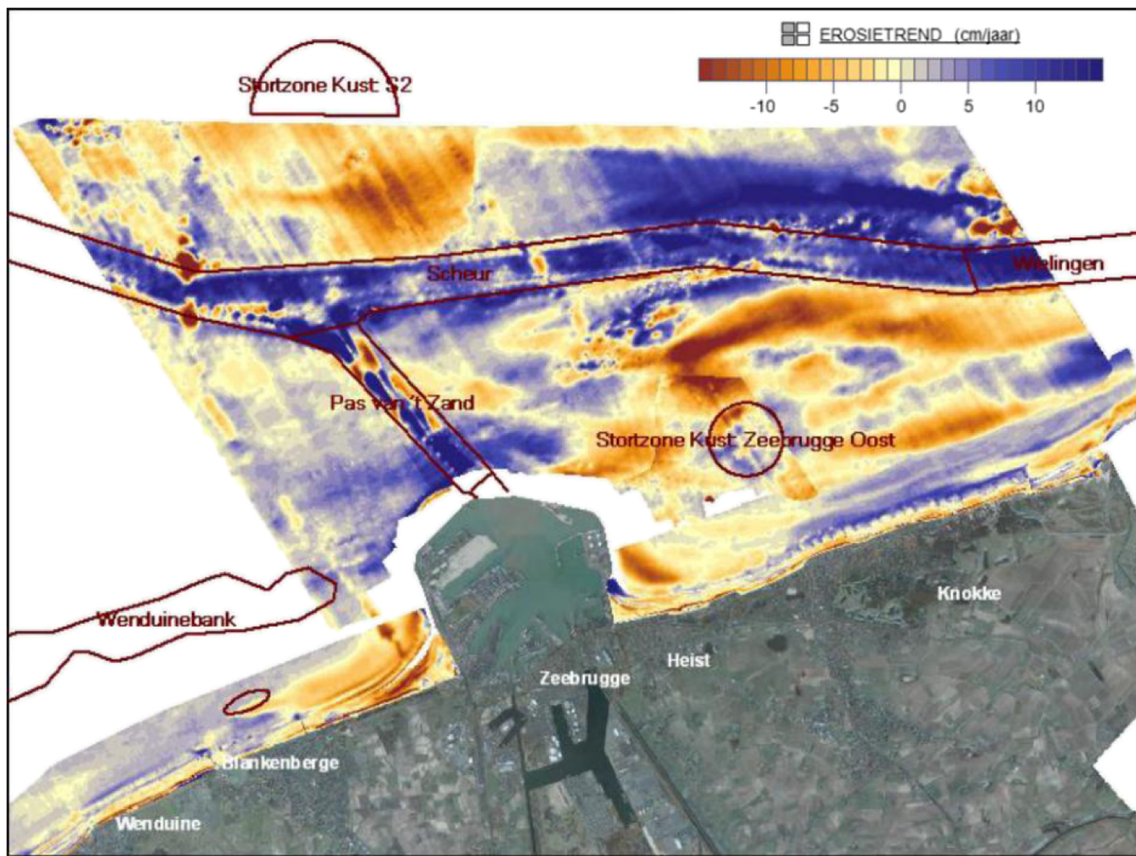


**Fig. 34** Measured erosion and sedimentation near the Port of Zeebrugge between 1999 and 2009 (Janssens et al. 2012)

$$h_+ = \sqrt{3Uh/\nu} \tag{38}$$

Finally, the suspension viscosity  $\nu(\varphi)$  is a function of the suspension concentration and can be expressed empirically as:

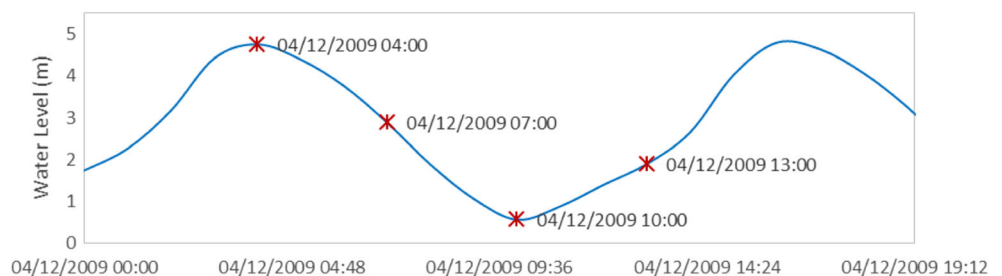
$$\nu(\varphi) = \nu_w \left( 1 + \frac{C_s}{C_{ref}} \frac{h}{h_{ref}} \right) \tag{39}$$

The empirical parameters ( $C_{ref}=0.222$  g/l and  $h_{ref}=0.12$  m) in Eq. 39 have also been obtained from calibration with the experimental data from Cellino (1998), shown in Fig. 7.

In summary, the dissipative effect of suspended sediment is incorporated into the closures for the effective roughness (which actually is a length scale related to the turbulent eddies generated by vortex shedding over roughness elements and in the wake of particles) and the suspension viscosity (e.g. including steric hindrance and granular friction of dense sand suspension or non-Newtonian behaviour of fluid mud).

Unlike in traditional hydrodynamic models (e.g. Hervouet 2007; Amoudry 2008), this new bottom-friction model accounts for the water depth and remains valid in turbulent, transient and laminar flows until an intertidal area falls dry. Due the fact that the classical friction law in traditional models is only valid for fully developed turbulent flow conditions, an inundation threshold has to be imposed, which keeps the water level

**Fig. 35** A typical tidal cycle in the Scheldt estuary





at a minimum height, to avoid numerical problems. When two neighbouring nodes with a different bottom level are in that state, a gravity driven flow will be induced from the node at higher elevation to the one at lower elevation. This artificial flow may become too strong and cause erosion, which does not occur in reality. The problem can be reduced by taking a high enough threshold value and/or by temporarily removing grid cells from the computational domain ('masking'). In practice, it turns out that there often remain nodes where the problem persists. The new friction law avoids this problem by increasing the roughness with decreasing water depth and the friction tends to infinity as soon as the inundation threshold, taken equal to the equivalent roughness height  $z_0$ , is reached, preventing flow. Masking is no longer necessary and mass conservation is much better guaranteed. Subsequently, the model allows a more accurate (and numerically stable) prediction of hydrodynamics over intertidal flats, since no inundation threshold needs to be specified any longer. Furthermore, for studying morphodynamics of the channel system in the estuary (e.g. the Scheldt estuary), a correct representation of residual flow circulations related to ebb and flood channels requires spatial and tidal phase dependent roughness values (Fokkink 1998), which makes this new bottom-friction model important for the coastal and estuarine studies. Figure 8 shows the spatial and temporal variations in Chézy coefficients obtained from this new bottom friction law. The different model behaviour is also clearly demonstrated in Fig. 9.

### 3 Calibration and validation

The model has been calibrated against the time series of measurements in 2009 at several locations both in the upstream and in the downstream near the Belgian coast. The available data sets are provided by the Royal Belgian Institute of Natural Sciences, Operational Directorate Nature (former Management Unit of the North Sea Mathematical Models and the Scheldt estuary, MUMM), Flanders Hydraulics Research (Waterbouwkundig Laboratorium) and IMDC, Belgium, and Rijkswaterstaat, Centre for Water Management, The Netherlands.

The measurements close to the Port of Zeebrugge are taken and processed under the framework of 'Monitoring and modelling of cohesive sediment transport and evaluation of the effects on the marine ecosystem as a result of dredging and dumping operations' (MOMO) by MUMM and RV Belgica in the period January to December, 2009 (Backers and Hindryckx 2010). There are four field campaigns carried out and during these campaigns, water level, flow velocity and direction, and turbidity, are continuously measured as well as some basic parameters (temperature, salinity, density, fluorescence and meteorological data) during one or several measurement cycles. In addition, the necessary water samples are taken for calibration. The measurement locations are indicated in Fig. 10, and their coordinates are given in Table 2. These data are mainly used for calibration of the suspended-sediment concentration and salinity near the Belgian coast.

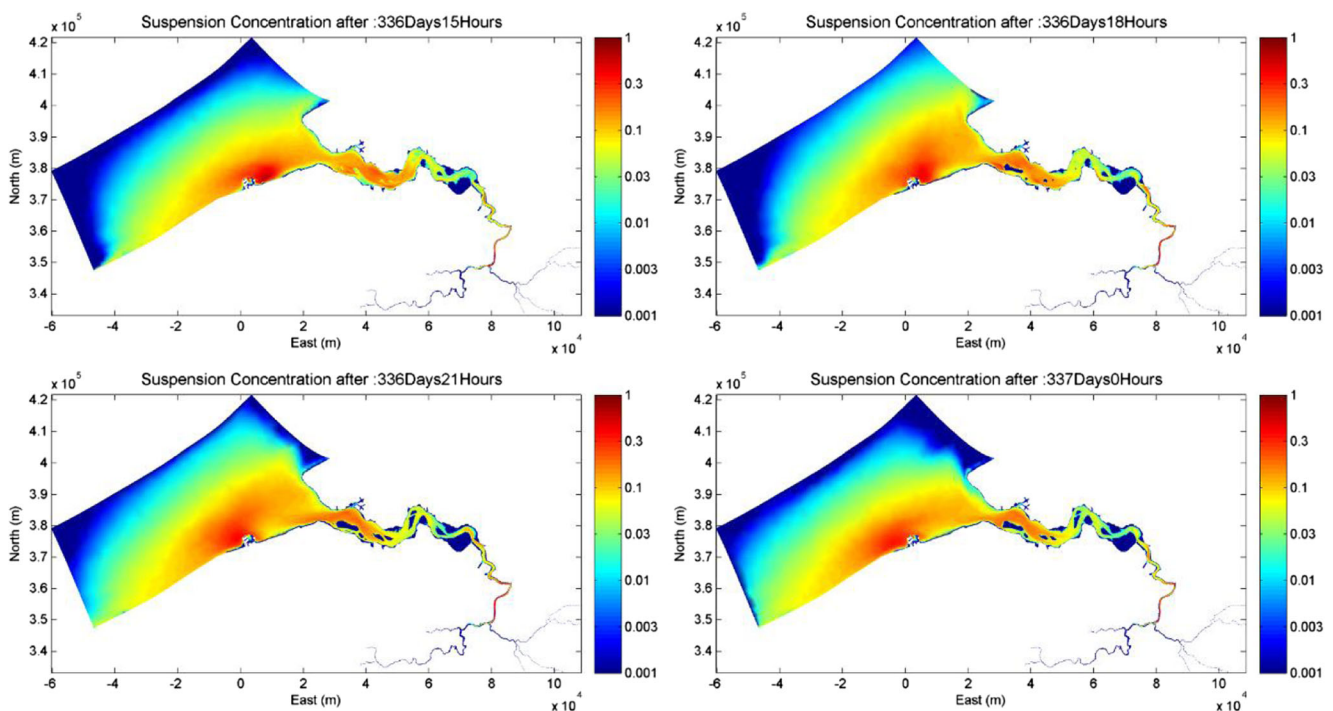


**Fig. 36** Suspension concentration (g/l) evolving within a typical tidal cycle

Rijkswaterstaat, Centre for Water Management, The Netherlands, has the monitoring network all over the Scheldt estuary, but those measurements are mainly water level, temperature and wind speed. The time series of measurements can be downloaded from the WTZ database in the Hydro Meteo Centrum (<http://www.meetadviesdienst.nl/nl/water-en-weer.htm>). Thus, these data sets are used to calibrate the hydrodynamics in the coastal areas and as a

complementary to MUMM data. The measurement locations in the interested area are indicated in Fig. 11, and their coordinates are given in Table 3.

The third set of measurements mainly located in the upstream of Scheldt close the Port of Antwerp, carried out by Flanders Hydraulics Research and IMDC, under the project ‘Prolonged measurements in Deurganckdok: Follow-up and accretion analysis’, which is the long-term measurements

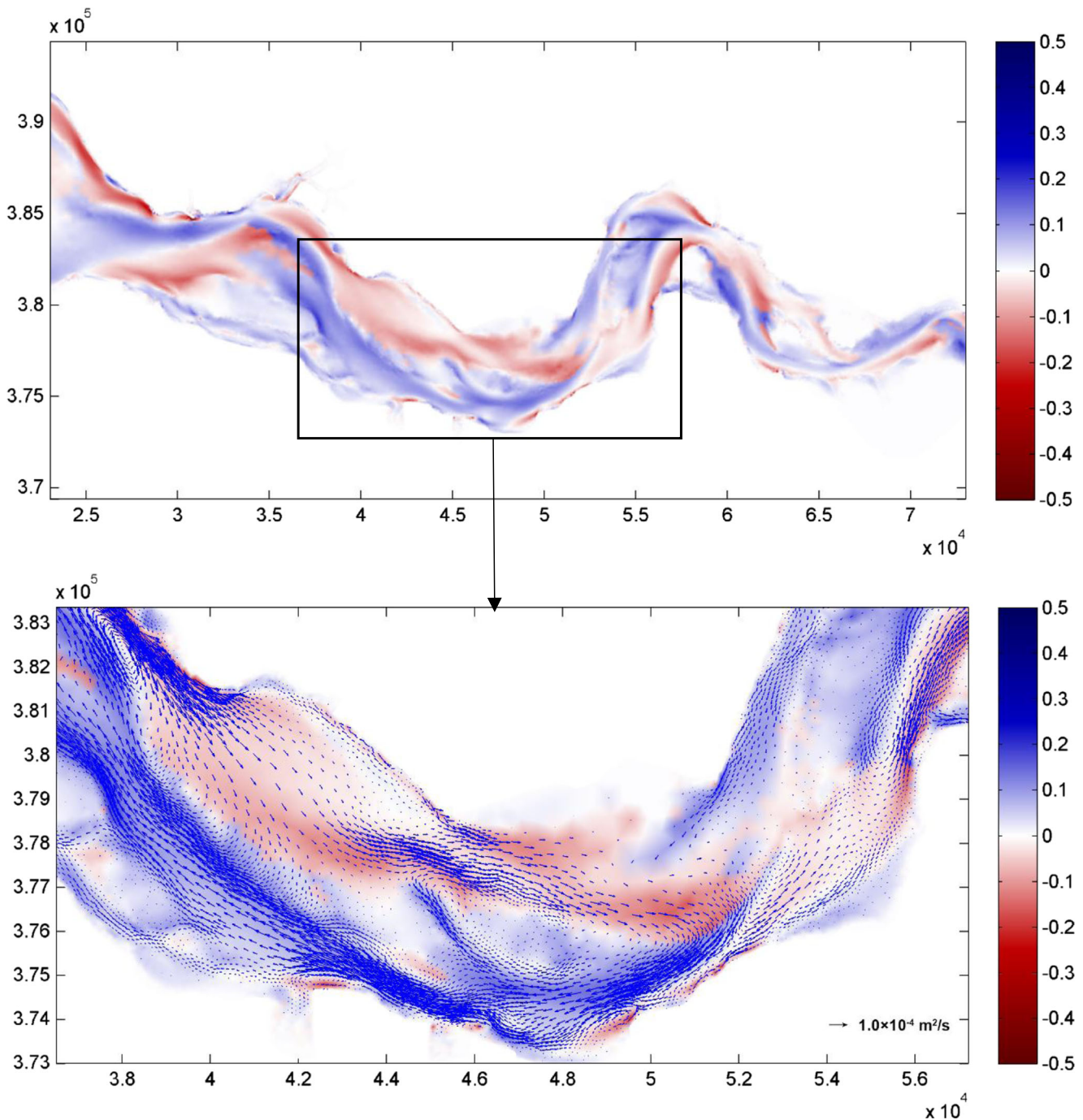
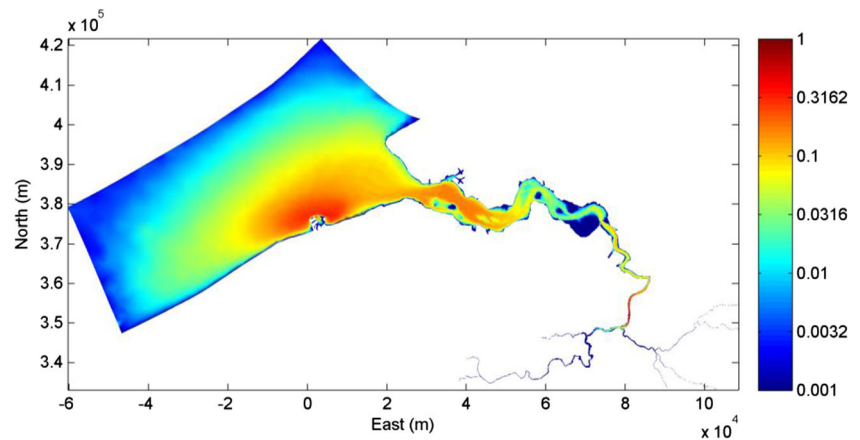


**Fig. 37** Computed residual velocity (m/s, *upper figure*) and the bedload transport (m<sup>2</sup>/s, *lower figure*) over a period of 1 year. The *red areas* indicate the flood-dominated channels, and the *blue areas* are the ebb-

dominated channels. It also reveals the sediment circulation patterns and residual transport paths in the Temeuzen section of the Scheldt estuary

**Fig. 38** Suspended sediments concentration (g/l) from ConR case averaged over one tidal cycle



conducted in Deurganckdok aiming at the monitoring and analysis of silt accretion (International Marine and Dredging Consultants et al. 2010). This measurement campaign is an extension of the study ‘Extension of the study about density currents in the Beneden Zeeschelde’ as part of the Long-Term Vision for the Scheldt estuary. The available measurements are in the period April 2008 to March 2009, including upstream discharge in the river Scheldt; salt and sediment concentration in the Lower Sea Scheldt taken from permanent data acquisition sites at Oosterweel, Prosperpolder and up- and downstream of the Deurganckdok; near-bed processes in the central trench in the dock, near the entrance as well as near the landward end; near-bed turbidity, near-bed current velocity and bed elevation variations; current, salt and sediment transport at the entrance of Deurganckdok and vertical sediment and salt profiles recorded with the SiltProfiler equipment; and dredging and dumping activities. The measurement locations are indicated in Fig. 12, and their coordinates are given in Table 4. These data sets contain the measurements of water level, velocity magnitude, salinity level and suspension concentration in the simulation period 2009.

The calibration is carried out for the hydrodynamic model first, since the flow conditions are crucial for the sediment

transport. The main parameter calibrated at this step is the bottom friction coefficient (expressed in terms of a Chézy coefficient). The sediment transport model is considered reliable only when realistic flow conditions can be reproduced. The following features are most valued when evaluating the hydrodynamic model:

- The free surface elevation at the tidal cycle and seasonal time scales
- The magnitude of the velocity at different locations
- The salinity level in the mixing zone and in the coastal area.

Once the validity of the hydrodynamic model has been assured, it is then coupled with the sediment transport model for further calibration, since the implementation of the new friction law and the bed evolution will also alter the flow conditions to a certain extent. This time the calibration not only focusses on the hydrodynamics but also on the suspended-sediment concentration (The depth-averaged results have been converted based on Fig. 13 in order to be in accordance with data measured at different depths). The critical shear stresses for erosion of sand and mud, as well as their erosion constants are the main parameters for calibration

**Fig. 39** Suspended sediments concentration (g/l) from DepR case averaged over one tidal cycle

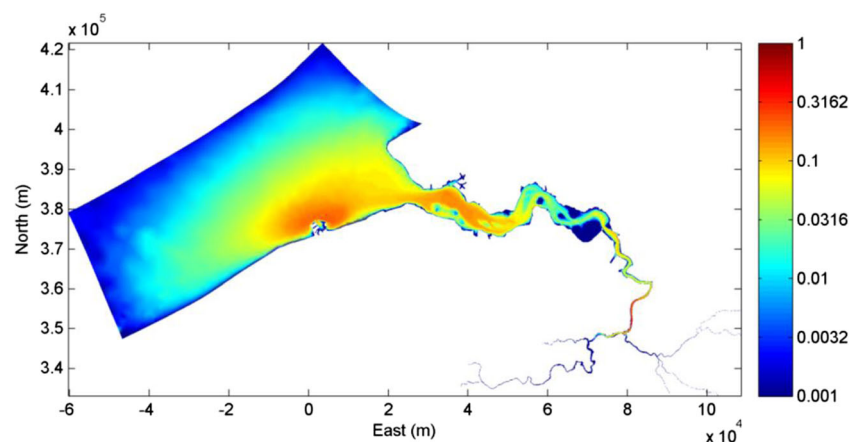
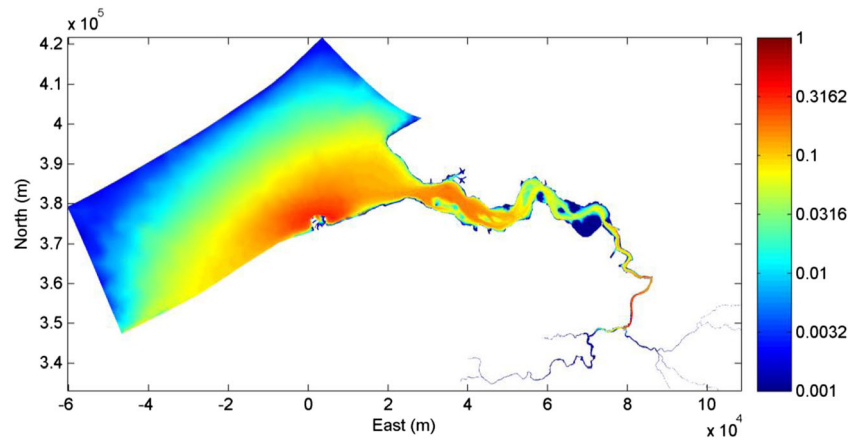




**Fig. 40** Suspended sediments concentration (g/l) from DepCsR case averaged over one tidal cycle



during this step. The model is evaluated as effective if the following features can be accurately represented:

- The order of magnitude of the suspended-sediment concentration throughout the estuary system
- The tidal and seasonal variations of the suspended-sediment concentration
- The turbidity maximum areas in the estuary.

The model incorporated with the new friction law, including the concentration effects, is used during the calibration and validation processes because it is more physics based and it is likely to perform better. For the hydrodynamics in the Scheldt estuary, water level, magnitude of velocity and salinity level are shown in Figs. 14, 15, 16, 17, 18, 19, 20, 21, 22, 23, 24, 25, 26, 27, 28, 29, 30 and 31 with comparison to the measured data.

In general, the water levels obtained from the model show good agreement with the measured data throughout the estuary and the upstream river network. It is worth mentioning here that, once the new friction law is implemented, the model gives good predictions in terms of water levels without tuning of the bottom friction parameters for specific areas, since the depth dependence is dominant relative to the influence of the

roughness height  $k_s$ . The comparisons are performed at three locations (nodes 4448, 5482 and 8949) in the downstream near the coast and three locations (nodes 27326, 28492 and 30783) in the upstream, close to the Port of Antwerp. Van Kessel et al. (2006) reported the tidal range at Vlissingen during a typical spring-neap tide varies from 2.97 to 4.46 m. It first increases towards the upstream, as it is affected by convergence and reflection. At Schelle (upstream of Antwerp), the tidal range during a typical spring-neap tide varies from 4.49 to 5.93 m, which is larger than at the mouth. Further upstream, the tidal wave decreases due to dissipation. This characteristic is also reproduced by the model. The variations of the free surface at all these locations with the measured data are shown in Figs. 14, 15, 16, 17, 18 and 19. In the locations close to Vlissingen (nodes 4448, 5482 and 8949), the tidal range is around 2.8 m up to 4.9 m. This is smaller than the tidal range in locations in the upstream (nodes 27326, 28492 and 30783) before it reaches Schelle, which is from about 4.2 m to 6.0 m.

The measured velocity magnitude during the simulation period is available at four locations, two near the Port of Zeebrugge (nodes 779 and 814) and the other two (nodes 28492 and 30783) in the upstream close to the Port of Antwerp. Figures 20, 21, 22 and 23 show the simulation

**Fig. 41** Differences of suspension concentration (g/l) predicted in the DepR case compared with the ConR case over the same tidal cycle on 4th December 2009

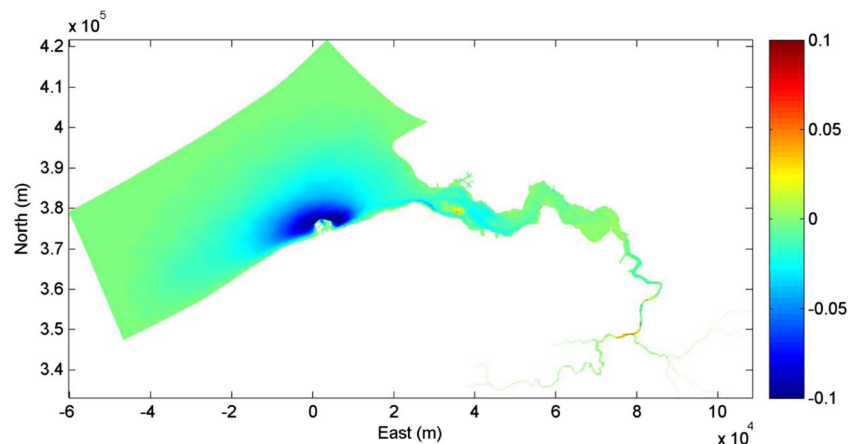
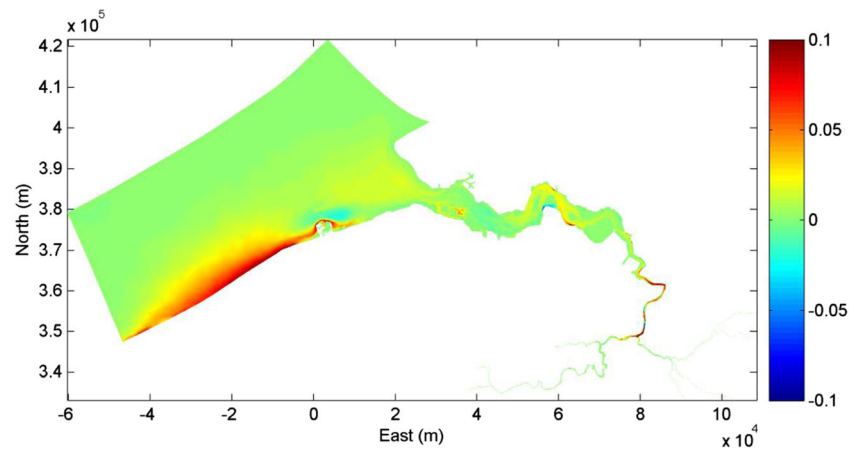


**Fig. 42** Differences of suspension concentration (g/l) predicted in the DepCsR case compared with the ConR case over the same tidal cycle on 4th December 2009



results compared with the measurements. The depths of measurements are given in Tables 2 and 4. The modelled depth-averaged velocities have been converted into the values at the corresponding depths (assuming a logarithmic profile) for proper model-data comparison. In general, the magnitude of the velocity obtained from the model is similar to the measurements except for the node 779, at which there is underestimation of the peaks during the high tide. The velocity in the upstream is larger than in the coastal area, which is consistent with the observations reported by van Kessel et al. (2006).

Three locations are selected to compare the salinity level from the results with the measurements. Node 814 is located in the coastal area near the Port of Zeebrugge (Figs. 24, 25 and 26). The time series of the measured data is available from February to April 2009. The salinity level near the Belgian coast is about 31 g/l. The underestimations of the peaks can be

easily seen at 14th and 30th of March, but in general, the simulated result matches the measurements at node 814. The other two locations (nodes 27326 and 28492) are in the partially mixed zone (Peters 1975; Nihoul et al. 1978) far away from the downstream. The salinity level in this area fluctuates between 6 and 10 g/l. The results show good agreement with the measured data at both nodes during that period. The more or less constant low value at ebb tide in these upstream nodes can be explained by the constant water discharge imposed as upstream boundary conditions, due to the lack of time series data.

The suspended-sediment concentration consists of the contributions from both cohesive and non-cohesive sediment. However, the concentration of suspended non-cohesive sediment is about two orders of magnitude lower compared to cohesive sediment, as expected. The results are plotted in

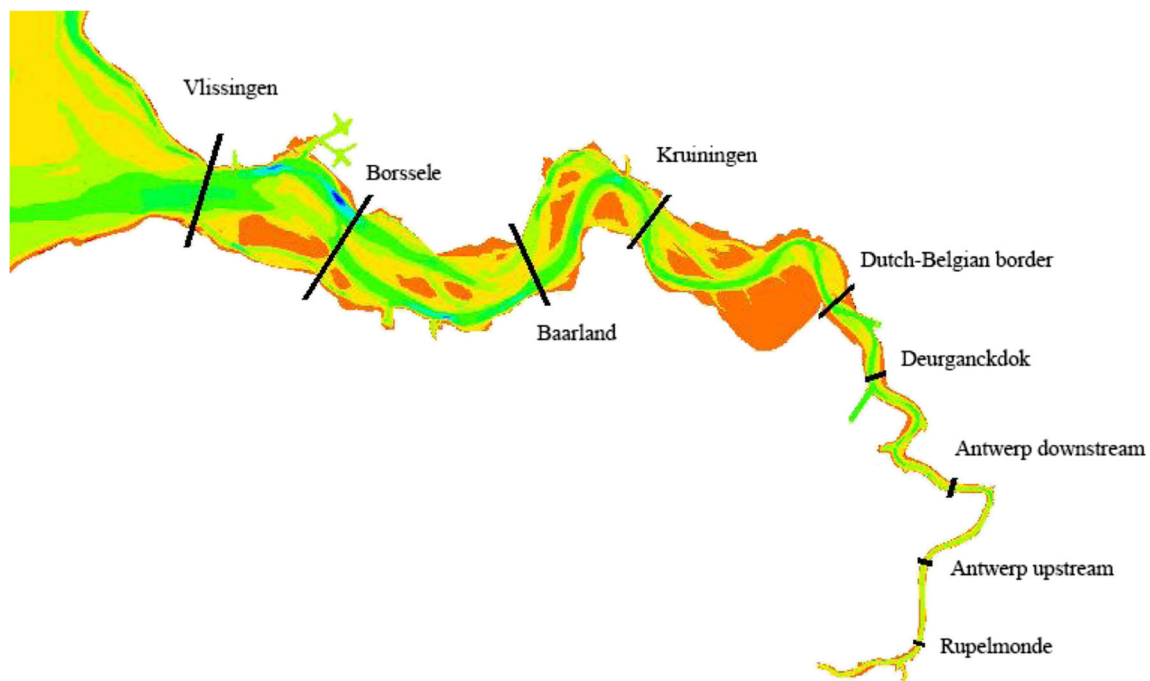
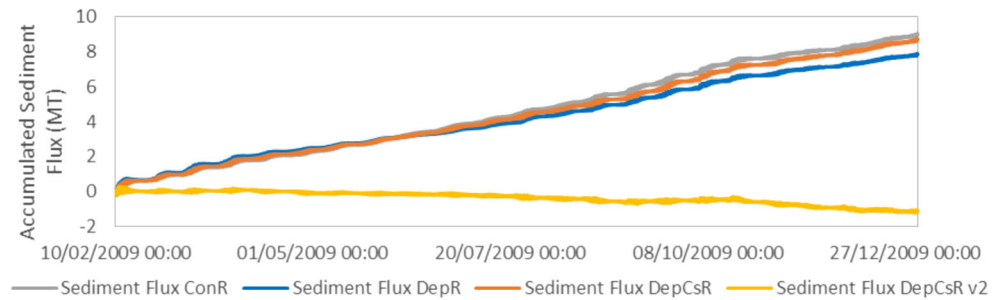


**Fig. 43** Transects defined in the model for calculating sediment fluxes



**Fig. 44** Comparison of accumulated sediment flux in 1 year at Vlissingen. The “v2” result is obtained by an assumed augmentation of the SPM concentration during floods with an average 12 % caused by wave-induced resuspension (see text for details)



Figs. 27, 28, 29, 30 and 31 with comparison with measurements at five locations (nodes 779, 814, 27326, 28492 and 30783). Again, for better comparison, the simulated depth-averaged concentrations have been converted into the values at corresponding depths based on the shape of the measured suspension concentration profile of Fig. 13. In general, the magnitude of the suspension concentration approximately matches the measured data. There are some deviations in the results, e.g. underestimations of the peaks at certain time steps. But, considering that the model is depth-averaged and without coupling with the wave model, which becomes important in the coastal areas, this is not surprising. The phases of the time series of suspension concentration generated by the model show good agreement with measurements while the underestimation of peaks most likely can be explained by lack of wave action, which is ignored in this study.

It is worth pointing out that, in the upstream locations, especially in nodes 28492 and 30783, the simulated suspension concentration rapidly decreases after reaching the peaks, while the measurements tend to maintain higher concentration for longer period. Taking into account the locations, a possible explanation could be disturbance by human activities. Nodes 28492 and 30783 are located in a busy navigation channel in the upstream. The comparison with measured data may indicate that the ship cruising, dredging or other activities during the period mid-January to late March were intensive and influenced the suspension concentration. After that, those activities seem to have reduced, and the suspended sediment was also less disturbed, which could explain the better agreement with data at the end of March in all three upstream locations.

Besides the calibration against the point measurements, the spatial variability of the suspended-sediment concentration has also been examined. In the Scheldt estuary, the turbidity

maximum zone is observed in different regions where a large amount of cohesive sediment particles are accumulated. These sediments are continually deposited and resuspended by the tidal flow. The distribution of suspended matter is influenced by a range of interrelated processes, e.g. temperature and biological activity, fresh water discharge and salinity, hydrodynamic conditions and turbulence, mineralogical composition, chemical conditions, aggregation and flocculation (Meire et al. 2005).

Three turbidity maximum zones can be observed in the Scheldt estuary, one in front of the Belgian coast around the Port of Zeebrugge, one at the freshwater/seawater interface in the downstream and a third one situated at about 50–110 km from the mouth originating from tidal asymmetry (Baeyens et al. 1998; Fettweis et al. 1998; Herman and Heip 1999). As indicated in Fig. 32, these turbidity maximum zones are reproduced by the model.

The Port of Zeebrugge is a major port in Europe and also an important multifaceted port in north-western Belgium. For better port management and toward sustainable development, many research tools were developed for investigating the flow conditions and sedimentation around Zeebrugge, in order to provide scientific advice to policy makers by simulating many different scenarios. In order to evaluate the quality of the model particularly in this area, the erosion and sedimentation around the Port of Zeebrugge after 1 year simulation is carefully examined. The reference data are from the Quest4D project in which they measured topography and bathymetry changes over the period 1999–2009 and observed long-term morphological evolution of the Belgian coast and shelf (Janssens et al. 2012). Comparing the modelled erosion and sedimentation patterns with the measurements (Figs. 33 and 34), many similarities can be discovered. Erosion occurs along

**Fig. 45** Comparison of accumulated sediment flux in 1 year at Borssele

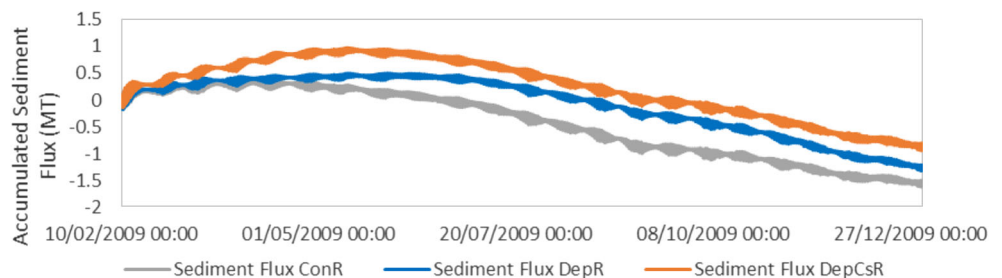
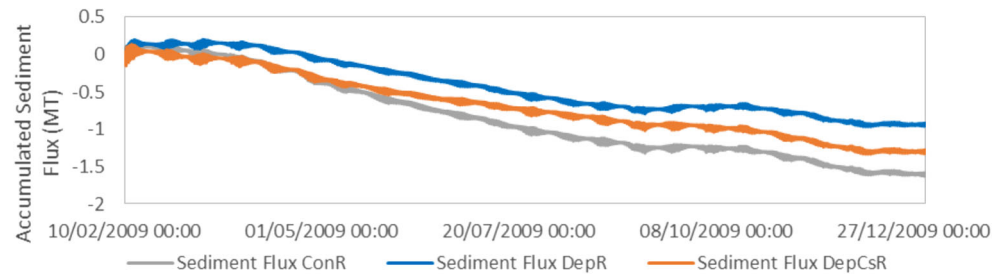


**Fig. 46** Comparison of accumulated sediment flux in 1 year at Baarland



the two breakwaters and develops towards the sea. The sedimentation zone appears on the right side of the port. These two patterns can be observed in both models. The most obvious difference is that the sedimentation also develops inside the port near the entrance to the sea, while it is not the case in the N2V model. Since our model has not been optimised for the nearshore, there remains still some potential for future improvements.

#### 4 Results

The calibrated model is then used to investigate the sediment transport in Scheldt Estuary and, more importantly, to quantify the concentration effects in the new bottom friction law and its influence on the sediment flux.

In one tidal cycle on 4th December 2009 as indicated in Fig. 35, the evolution of sediment concentration can be seen in Fig. 36. The model shows that the movements of the turbidity maximum near the Port of Zeebrugge are always counter-clockwise. Sediment is accumulated at the east side of the port, then transported around the port towards the south-west and finally stays at the west side of the port. This is consistent with the erosion and sedimentation patterns found in the observations (Janssens et al. 2012) and the modelled results (Figs. 33 and 34). For the turbidity maximum in the upstream, its movement seems to react rapidly to the tidal waves. During the ebb tide, the turbidity maximum shifts towards the downstream and then shifts backwards during the flood tide.

The model also shows the ability to represent the residual flow circulations related to ebb and flood channels. Figure 37 reveals the flood/ebb channel system in the Terneuzen section of the Scheldt estuary, which is in good agreement with the

study of Jeuken (2000). According to her study, the flood/ebb channel system is responsible for the residual sediment transport patterns found in the Scheldt, i.e. the sediment circulation and the transport paths. More sediment is transported landward in the flood channels and seaward in the ebb channels during a tidal cycle. This is also helpful for explaining the erosion/sedimentation occurring in the Scheldt.

For the purpose of demonstrating the new physics-based bottom friction law, two more test cases were created besides the standard model. The standard model incorporates the full version of the new friction law including the concentration effects and is denoted as the DepCsR. The other two are the test case with constant roughness coefficient (Chézy coefficient=65, obtained by calibration with water depth data, denoted as ConR) and the test case with the new friction law excluding the concentration effects (denoted as DepR). The rest of the model settings are identical in all the test cases.

The suspended-sediment distributions from all three cases averaged over the same tidal cycle on 4th December 2009 are put together for comparison. As it can be seen from Figs. 38, 39 and 40, similar sediment distribution patterns are found in both the ConR and DepR cases. However, the suspension concentration in the North Sea and in the upstream close to the port of Antwerp is reduced with the simplified version of the new friction law (without the concentration effects). In the DepR case, less suspended sediment appears in the river mouth. It also does not reach the south-west of the port of Zeebrugge as far as the ConR case. The DepCsR case shows a different sediment transport pattern compared with other two cases. In general, higher suspension concentrations are obtained with the new friction law including the concentration effects, especially near the coast and in the upstream. The suspended sediment spreads further near the coastal area and

**Fig. 47** Comparison of accumulated sediment flux in 1 year at Kruiningen

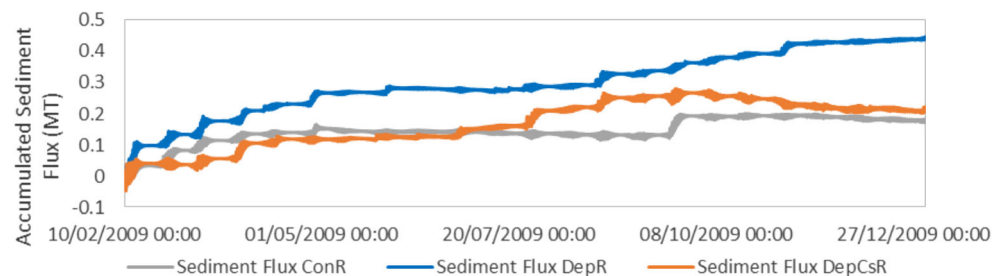
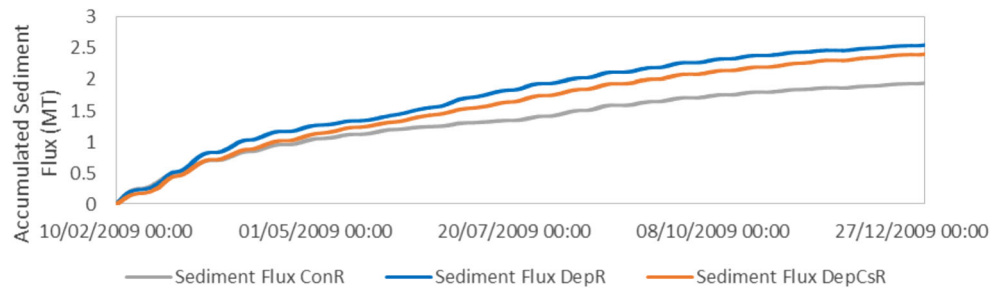


**Fig. 48** Comparison of accumulated sediment flux in v at Dutch–Belgian boarder



the turbidity maximum close to the port of Antwerp also extends further towards the downstream, which is closer to the observations.

Differences of averaged suspension concentration over the same tidal cycle between DepR and the ConR cases are shown in Fig. 41 and the differences between DepCsR and the ConR cases in Fig. 42. Positive values mean higher concentration compared to the ConR case and vice versa. Figure 41 shows that the new roughness law without considering the concentration effects used in the DepR case predicts less suspended sediment around the Port of Zeebrugge than using constant roughness in the ConR case. There are also underestimations in the navigation channels near the river mouth compared with ConR case, while the concentration level in the turbidity maximum area close to Antwerp is higher. The better model performance can be clearly seen in the DepCsR case (Fig. 42) with the new roughness law including the concentration effects, in which both the predictions in the upstream turbidity maximum zone, as mentioned earlier, and the predicted concentration levels of suspended sediment in the coastal area have been improved. As indicated in Fig. 36, the suspended sediment is brought up from the northeast of the Port of Zeebrugge and then transported along the Belgian coast towards the southwest in within a tidal cycle. The excessive concentration in the coastal area shown in Fig. 42 implies that the suspended sediments can be transported further southwest along the coast in the DepCsR case than the ConR case. This trend is confirmed by the processed SeaWiFS remote sensing images by (Fettweis et al. (2007), which shows the seasonal averages (winter situation, similar as in Figs. 38, 39, 40, 41 and 42) of vertically corrected SPM concentration in the southern North Sea.

In addition to the suspension concentration, the sediment flux has also been examined. Again, the results from all three cases were analysed and compared. For a better understanding of the sediment circulation in the Scheldt, the entire research domain has been divided by nine transects (Fig. 43). The accumulated sediment fluxes were calculated and plotted in Figs. 44, 45, 46, 47, 48, 49, 50, 51 and 52. The positive value means the sediment flux has a direction normal to the transect pointing to the downstream (seaward), while the negative value means the opposite direction (landward).

The initial (model warming-up) period (the first 40 days of the year) for each case is eliminated in order to avoid its influence. All the sediment fluxes start from zero at 00:00:00, 10th February 2009 and accumulate over time. The results explain how the turbidity maximum areas are formed in the River Scheldt. The turbidity maximum near the river mouth is caused by the sediment fluxes coming from two opposite directions—suspended sediment being transported upstream at Borssele and transported downstream at Kruiningen; finally, they converge at the locations in between, shifting back and forth due to the flood or ebb tide. Another turbidity maximum is formed in the same way. The sediment flux is towards the upstream at Deurganckdok, joining the sediment flux in the opposite direction from upstream Antwerp. The reason behind the sediment flux coming from different directions could be the tidal asymmetry—the non-linear processes governed by the basin morphology when astronomic tidal waves propagate into the estuary (Bolle et al. 2010). For this particular case, the horizontal tide is considered as asymmetric since the differences can be easily found between the ebb and flood velocities from the results. Figures 53 and 54 show the velocity components at node

**Fig. 49** Comparison of accumulated sediment flux in 1 year at Deurganckdok

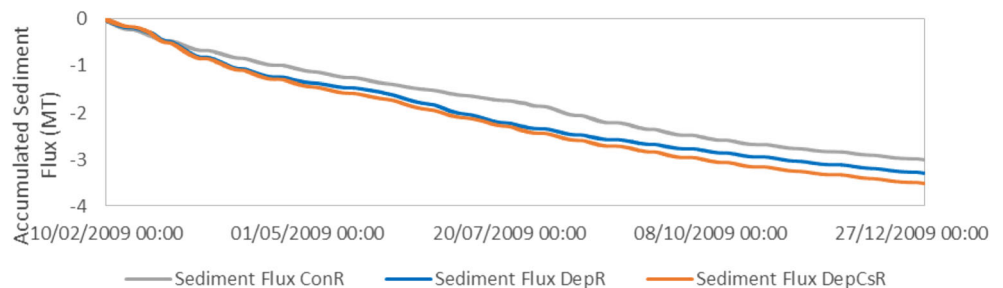
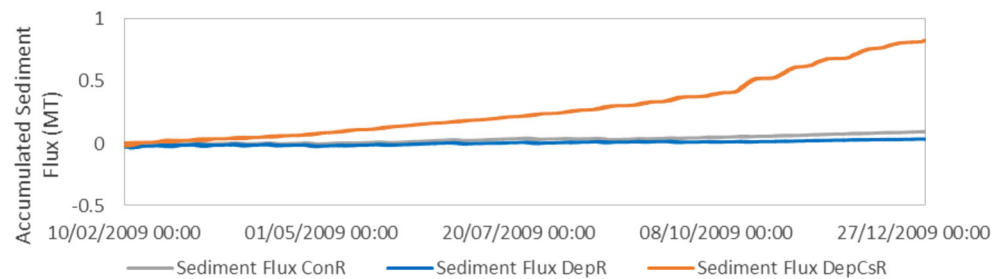


**Fig. 50** Comparison of accumulated sediment flux in 1 year downstream of Antwerp City



28492 (in the downstream of Deurganckdok) from 6000 to 7000 h of the simulation. The velocity components are asymmetric in both directions, and the magnitude of the velocity towards upstream is almost 30–40 % larger than the opposite direction. It also reveals that the sediment flux is already in the upstream direction before reaching the transect at Deurganckdok.

Comparing the calculated sediment fluxes in all three cases at each transect does not give clear insight on how the new bottom friction law affects the sediment flux at a particular place. It is also determined by the bottom topography, flow conditions and many other factors. But one thing is sure, that the concentration effects cannot only alter the distribution of suspended sediments in the estuary but also have an influence on the sediment flux in the entire domain and it tends to be more important in the upstream.

The mass balance for the Scheldt estuary is one of the enigmas that still is not resolved. A few attempts have been carried out in the 1990s, which suggest a small yearly import of mud from the sea into the Western Scheldt where it deposits (Wartel and van Eck 2000). The most recent data and simulations suggest that the net inflow of fine-grained sediment during flood is of the same order of magnitude as the outflow during ebb (order 400 ktons/day; van Kessel and Vanlede 2010). These results are confirmed by the present model. However, the residual transport over a tidal cycle is the difference between nearly equally large numbers and very sensitive to proper model settings. Estimations based on the change in bottom topography over many years and a known inflow from the continental side suggest confirmation of the earlier trend of net import of mud over the transect Vlissingen–Breskens, increasing in recent years, attributed to the subsequent

deepenings (Dam and Cleveringa 2013). However, the mud transport model set up by Deltares, without morphodynamics, predicted a small net export for the year 2006 (van Kessel and Vanlede 2010). The present model, the first one accounting simultaneously for both sand and mud transport and including morphodynamics, even predicts a net export roughly five times larger over the year 2009.

In order to trace the likely reason for the discrepancy, despite the overall good predictions of the model, a sensitivity analysis has been carried out for an arbitrary tidal cycle near the end of the simulation. The simulated sediment flux (positive sign means exporting seaward, and vice versa) passing through the Vlissingen–Breskens transect at the end of December 2009 is shown in Fig. 54. For this particular cycle, the net export of mud is found to reach roughly 30 ktons/cycle. The export is simply explained by the fact, that during flood, the flow velocity is lower than at ebb, while the flood SPM concentration varies between 90 and 120 mg/l, whereas the ebb SPM varies between 100 and 140 mg/l. These values lie in the range of the few scattered data available, giving an average of 130 mg/l (van Kessel et al. 2011). With only a slight increase of on average 20 % in the mud SPM during flood, the residual flux over one tide reverses sign. Unfortunately, there are no systematic SPM measurements over a tidal cycle available for this location at the moment. However, it can easily be imagined that the SPM values at the sea side are underestimated in the model since resuspension by waves has not been modelled.

In Fig. 55, the total SPM with wave-induced resuspension is approximated heuristically (using a weak power law function), allowing the SPM to increase gradually during the flood tidal phase when the flow moves landward. This time, the

**Fig. 51** Comparison of accumulated sediment flux in 1 year upstream of Antwerp City

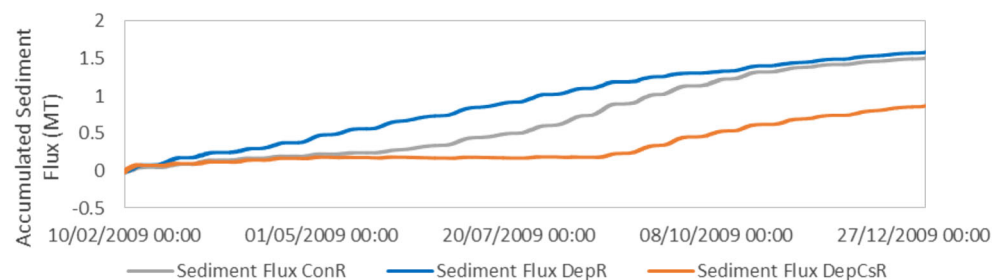
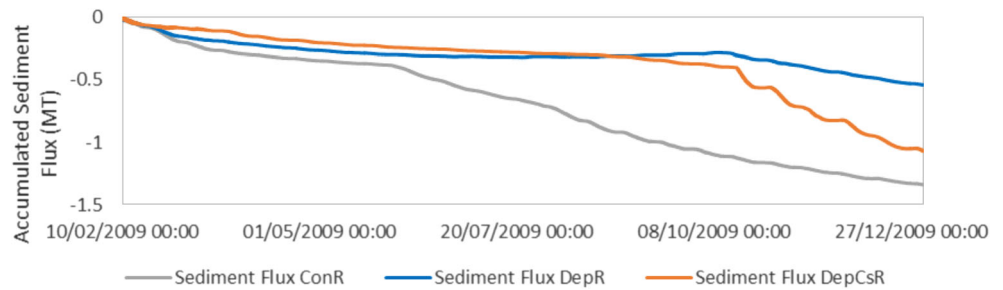




**Fig. 52** Comparison of accumulated sediment flux in 1 year at Rupelmonde



cumulated sediment flux (1.6 kt/cycle or 1.17 Mt/year) reverses the residual flux direction to import from the seaside, and its value is also much closer to the one found in the latest study for the Flemish-Dutch Scheldt Commission (VNSC: Vlaams-Nederlandse Scheldecommissie) (Cleveringa 2013) where the conclusion is a net import of the order 0.75 Mm<sup>3</sup>/year, which corresponds to 0.9–1.2 Mt/year (depending on the assumed mud density). To obtain the same net flux over the entire year 2009, the seaward concentration needs an average increase of only 12 % (Fig. 44). These computations show the high sensitivity to assumptions and calculation procedures.

Notice that in other two transects upstream of Vlissingen–Breskens, the simulated sediment fluxes (Figs. 45 and 46) are much closer to the values found in the VNSC study (Cleveringa 2013) at the similar cross-sections in terms of both direction and magnitude (0.8–1.1 Mt/year at both Borssele and Baarland, import from the seaside), which suggests that this kind of impact on the net sediment flux is specifically important in the coastal areas up to the river mouth and becomes very limited in the upstream. This makes the assumption about the behaviour of the wave-induced sediment flux more logical.

However, the simulated results on sediment fluxes may not necessarily correspond to reality. The reason for caution is the fact that the transport in the present 2DH model is governed by the depth-averaged velocity. For instance, in the present 2DH model the bedload transport shows the same accumulated flux pattern as the suspended load, which is not as expected. In reality, the transport at the surface may go in the opposite direction relative to the near-bottom and bedload transport as a result of freshwater–seawater interaction and inertia.

Therefore, it is strongly recommended to set up a 3D model where surface and bed currents can be computed individually, before drawing conclusions on actual residual fluxes, their direction and magnitude.

### 5 Conclusion

The KU Leuven–Télémac Western Scheldt model has been established and used as the first high resolution mixed-sediment transport model to study the transport patterns and sediment flux in the Scheldt estuary. A new physics-based friction law, based on a generalised mixing-length theory (GML), has been incorporated in this model. A new deposition criterion based on a suspension capacity condition has been implemented as well. The critical shear stress for deposition is no longer taken constant, but related to the available energy for suspending particles. Its instantaneous value is obtained from the local suspension capacity condition. It is no longer a pure material parameter but a function of sediment concentration, settling velocity, water depth and bed shear stress. The model deals with two types of sediments, sand and mud, and the bed composition of the entire domain is defined non-uniformly based on survey data. A unified way of calculating erosion/deposition was used in this study. The model has been calibrated against measurements at different locations and is able to reproduce a realistic flow field in general. Due to the complexity of the research domain, more data are required for further improvement.

Numerical simulations have been carried out to compare and analyse the model results obtained for different friction

**Fig. 53** Velocity component *U* in X direction at node 28492 from 6000 to 7000 h

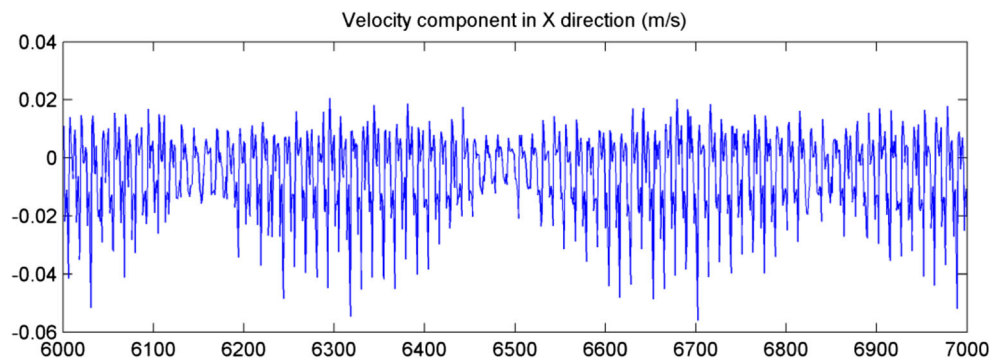
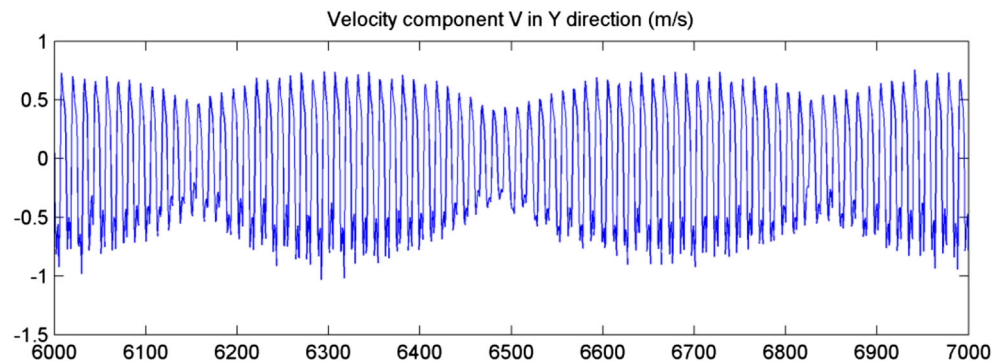


**Fig. 54** Velocity component  $V$  in  $Y$  direction at node 28492 from 6000 to 7000 h



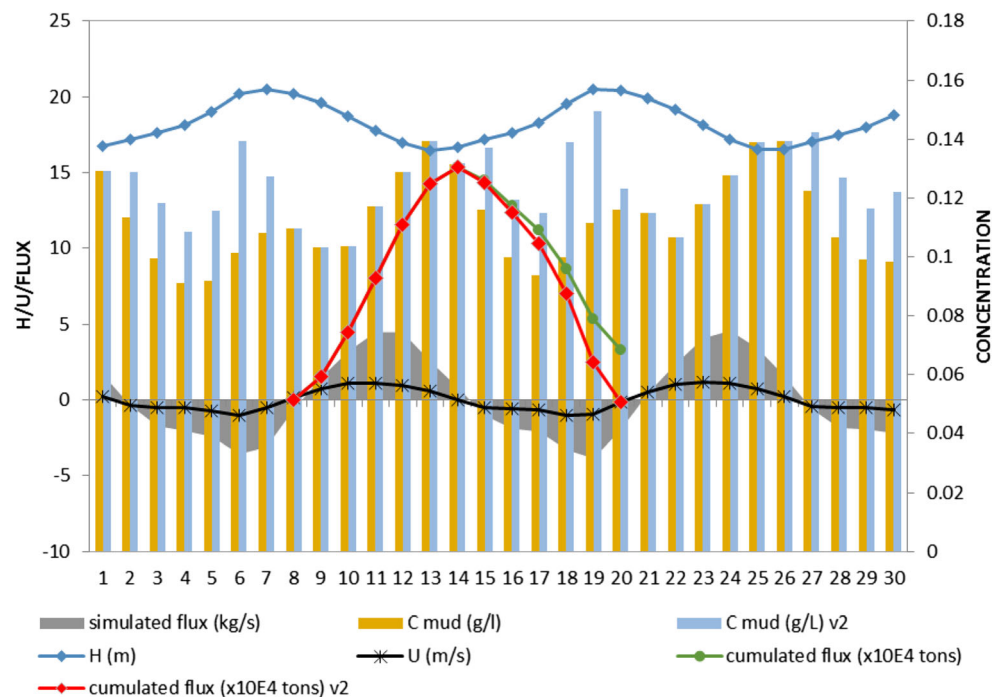
laws. Three bottom friction laws have been implemented and applied to the same test case (identical model set-up and initial conditions), partially calibrated and validated with field data from 2009. The first model applies a constant roughness coefficient, which at present is the most current practice in engineering studies. The second model employed a depth-dependent formulation, obtained by integration of the standard logarithmic velocity profile (Prandtl–von Karman). The third model is an extension of the second, including viscous stresses, effective bed roughness (dissipation by separation vortex generation) and additional dissipation mechanisms that become important in high-concentrations as found above the bed (i.e. interparticle friction and collisions, and particle wake turbulence) resulting in a bed shear stress predictor. In each case, the computed friction has been converted into an equivalent Chézy friction coefficient. The comparison of all the three cases shows that the third model has better predictions in terms of distributions of suspended sediments in the Scheldt estuary, especially in the turbidity maximum zones in the

upstream and the general transport patterns near the Belgian coast. It also demonstrates that the sub-grid-scale effects, such as additional viscous stresses and dissipation mechanisms induced by sediment particles, etc., in the high concentrated layer are important and indeed have big influence to the large-scale domain.

Since the new bed shear stress closure is constructed as the superposition of the turbulent and the laminar part, it allows the simulation of both transient conditions and the transition during drying or wetting of tidal flats. Nikuradse's empirical roughness model is implemented allowing to account for both hydraulic smooth and hydraulic rough conditions. The latter is important since the tidal induced oscillatory flow may fulfil either condition, depending on the phase of the tidal cycle.

An additional advantage of the new friction law is the fact that its value automatically tends to infinity when the water depth goes to zero. Therefore, the drying and flooding of intertidal flats can now be modelled without specifying an inundation threshold. This proved to work very well for the

**Fig. 55** Hourly computed values of depth-averaged SPM concentrations and mud fluxes and effect of artificial increase of the flood SPM concentrations (indicated “v2”). Computed values of water levels and depth-averaged flow velocity are also shown. Results for a tidal cycle (from 2009–12–30, 1900 hours to 2010–01–01, 0000 hours) in a point roughly halfway in the cross-section between Vlissingen and Breskens at the mouth of the estuary. Cumulated fluxes are for the full cross-section



many intertidal areas in the Western Scheldt. The benefit is that intertidal morphodynamics can now be modelled at great detail for the first time. Erosion and deposition in these areas can now be estimated with much higher accuracy, as well as their contribution to the overall net fluxes. Besides, the new friction law can adapt to different topographies due to its physics based characteristics and provides the hydrodynamic model with better performance in terms of water levels and velocity field without tuning of the bottom friction coefficient.

The sensitivity of the model to the bed friction model has been evaluated by intercomparison of the computed sediment budget at the mouth of the estuary. This has always remained a point of discussion, since previous model results did not match with estimates based on field data, even opposite directions have been claimed. Near-bottom sediment transport, which is hard to model and which escapes from most measuring techniques, most likely plays an important role in explaining the differences. The comparison of the three friction models indeed results in different evolutions of the net sediment budget calculated at different transects across the entire estuary. These differences are also reflected in significant differences in local erosion-sedimentation patterns.

The asymmetrical tide is also reproduced in the model and could be interpreted as the main reason of the occurrence of the turbidity maximum areas in the Scheldt. The model captures the sediment fluxes from two different directions converging in the upstream and downstream, resulting in the accumulation of suspended sediment in those areas.

Nevertheless, the fact that the flow at the surface may be in opposite direction than the near-bottom current is expected to have a great impact on the actual residual fluxes of both suspended load and bedload. Therefore, it is necessary to develop a 3D version of the model, before any conclusions can be drawn on direction and magnitude of the fluxes. A 3D version of the present model is currently under development.

The model is expected to yield even better results when the dynamics of flocculation is incorporated, following the computational efficient methodology proposed by Lee et al. (2014).

**Acknowledgements** This study has been supported by the EU FP7 projects THESEUS and FIELD\_AC. The computational resources and services used in this work were provided by the VSC (Flemish Supercomputer Center), funded by the Hercules Foundation and the Flemish Government—department EWI.

## References

- Amoudry L (2008) A review on coastal sediment transport modelling. POL Internal Document No.189, Proudman Oceanographic Laboratory, Liverpool, 44
- Backers J, Hindryckx K (2010) RV Belgica: rapport van de RV Belgica meetcampagnes en verankering van meetsystemen MOMO—2009. Beheerseeneheid Mathematisch Model Noordzee. Meetdienst Oostende, different pagination + data CD-ROM (in Dutch)
- Baeyens W, Adam Y, Mommaerts JP, Pichot G (1981) Numerical simulations of salinity, turbidity and sediment accumulation in the Scheldt estuary. Elsevier Oceanography Ser 32:319–332
- Baeyens W, Van Eck G, Lambert C, Wollast R, Goeyens L (1998) General description of the Scheldt estuary. Hydrobiologia 366:1–14
- Bolle A, Bing Wang Z, Amos C, De Ronde J (2010) The influence of changes in tidal asymmetry on residual sediment transport in the Western Scheldt. Cont Shelf Res 30(8):871–882
- Cancino L, Neves R (1994) 3D-numerical modelling of cohesive suspended sediment in the Western Scheldt estuary (The Netherlands). Neth J Aquat Ecol 28(3–4):337–345
- Cancino L, Neves R (1999a) Hydrodynamic and sediment suspension modelling in estuarine systems: part I: description of the numerical models. J Mar Syst 22(2):105–116
- Cancino L, Neves R (1999b) Hydrodynamic and sediment suspension modelling in estuarine systems: part II: application to the western Scheldt and Gironde estuaries. J Mar Syst 22(2):117–131
- Cellino M (1998) Experimental study of suspension flow in open channels. PhD dissertation, No. 1824, Ecole Polytechnique Fédérale de Lausanne
- Cleveringa J (2013) Grootchalige sedimentbalans van de Westerschelde. VNSC Basisrapport grootchalige ontwikkeling G-2. Report 076945827:0.4, Arcadis Nederland, Arnhem (NL), 81 pp
- Da Silva PA, Temperville A, Seabra Santos F (2006) Sand transport under combined current and wave conditions: a semi-unsteady, practical model. Coast Eng 53(11):897–913
- Dam G, Bliet AJ (2013) Using a sand–mud model to hindcast the morphology near Waarde, The Netherlands. In: Proceedings of the Institution of Civil Engineer. Mar Eng 166 (2):63–75
- Dam G, Cleveringa J (2013) De rol van het slib in de sedimentbalans van de Westerschelde. VNSC Basisrapport grootchalige ontwikkeling G-3. Report G3; 1630/U12376/C/GD, Svasek Hydraulics, Rotterdam (NL), 35 pp
- Dam G, Bliet AJ, Labeur RJ, Ides S, Plancke Y (2007) Long term process-based morphological model of the Western Scheldt Estuary. In: Dohmen-Janssen CM, Hulscher SJMH (eds) Proceedings of 5th IAHR Symposium of the River, Coastal and Estuarine Morphodynamics Conference, Enschede, The Netherlands, Vol. 2. Taylor & Francis, Leiden, The Netherlands, pp 1077–1084
- De Brye B, de Brauwere A, Gourgue O, Kärrn T, Lambrechts J, Comblen R, Deleersnijder E (2010) A finite-element, multi-scale model of the Scheldt tributaries, river, estuary and ROFI. Coast Eng 57(9):850–863
- De Ruijter, W, Huber, K, Backhaus, J (1987) North Sea circulation. In: Report of the Oceanography Subgroup. Second International Conference on the Protection of the North Sea, Scientific and Technical Working Group, pp. 19–36 (Chapter 4)
- Elghobashi S (1994) On predicting particle-laden turbulent flows. Appl Sci Res 52:309–329
- Fettweis M, Van den Eynde D (2003) The mud deposits and the high turbidity in the Belgian–Dutch coastal zone, southern bight of the north Sea. Cont Shelf Res 23(7):669–691
- Fettweis M, Sas M, Monbaliu J (1998) Seasonal, neap-spring and tidal variation of cohesive sediment concentration in the Scheldt Estuary, Belgium. Estuar Coast Shelf Sci 47(1):21–36
- Fettweis M, Nechad B, Van den Eynde D (2007) An estimate of the suspended particulate matter (SPM) transport in the southern north Sea using SeaWiFS images, in situ measurements and numerical model results. Cont Shelf Res 27(10):1568–1583
- Fokkink RJ (1998) Morphodynamic network simulations of the Western Scheldt. WL| Delft Hydraulics, Report Z, 919



- Gourgue O, Baeyens W, Chen MS, de Brauwere A, de Brye B, Deleersnijder E, Elskens M, Legat V (2013) A depth-averaged two-dimensional sediment transport model for environmental studies in the Scheldt Estuary and tidal river network. *J Mar Syst* 128: 27–39
- Hartsuiker G (2004) 2Dh NEVLA Scheldemodel: Bouw en afregeling stromingsmode (in Dutch). Report MOD 753. Antwerp, Belgium, Flanders Hydraulics Research
- Herman PMJ, Heip CHR (1999) Biochemistry of the maximum turbidity zone of estuaries (MATURE): some conclusions. *J Mar Syst* 22:89–104
- Hervouet JM (2007) Hydrodynamics of free surface flows: modelling with the finite element method. Wiley, Chichester
- Hervouet JM, Bates P (2000) The telemac modelling system. *Hydrol Process* 14(13), Special Issue
- Hoffmann M, Meire P (1997) De oevers langs de Zeeschelde: inventarisatie van de huidige oeverstructuren. *Water* 95:131–137
- Hoogduin L, Stive MJF, Wang ZB, Uijtewaai WSJ, Hibma, A, & Elkema, M (2009) Sediment transport through the Eastern Scheldt storm surge barrier. Delft University of Technology
- International Marine and Dredging Consultants et al. (2010) Langdurige metingen Deurganckdok: opvolging en analyse aanslibbing: deelrapport 1.23. Sedimentbalans 01/01/2009 - 31/03/2009. Versie 2.0. Waterbouwkundig Laboratorium: Antwerpen. IV, 28 + annexes (in Dutch)
- Janssens J, Delgado R, Verwaest T, Mostaert F (2012) Morfologische trends op middellange termijn van strand, vooroever en kustnabije zone langsheen de Belgische kust: Deelrapport in het kader van het Quest4D-project. Versie 1\_0. WL Rapporten, 814\_02. Waterbouwkundig Laboratorium: Antwerpen, België
- Jeuken MCJL (2000) On the morphologic behaviour of tidal channels in the Westerschelde estuary. *Nederlandse geografische studies* (Netherlands)
- Krone RB (1962) Flume studies of the transport of sediment in estuarial shoaling processes: Final Report. Hydraulic Engineering Laboratory and Sanitary Engineering Research Laboratory, University of California, 118 pp
- Kuijper C, Steijn R, Roelvink D, van der Kaaij T, Olijslagers P (2004) Report: Morphological modelling of the Western Scheldt: validation of Delft3D. *Deltares* (WL). Chapter 2, 1–2
- Lee BJ, Toorman E, Fettweis M (2014) Flocculation of fine-grained cohesive sediments developing multimodal particle size distributions: field investigation and mathematical modeling. *Ocean Dyn* 64:429–441
- Malherbe B (1991) A case study of dumping in open seas. *Terra et Aqua* 45, 5 – 32
- Maximova T, Ides S, De Mulder T, Mostaert F (2009a) Verbetering 2D randvoorwaardenmodel. Deelrapport 4: Extra aanpassingen Zeeschelde (in Dutch). WL Rapporten, 753\_09. Antwerp, Belgium, Flanders Hydraulics Research
- Maximova T, Ides S, Vanlede J, De Mulder T, Mostaert F (2009b) Verbetering 2D randvoorwaardenmodel. Deelrapport 3: Calibratie bovenlopen (in Dutch). WL Rapporten, 753\_09. Antwerp, Belgium, Flanders Hydraulics Research
- Meire P, Ysebaert T, Van Damme S, Van den Bergh E, Maris T, Struyf E (2005) The Scheldt estuary: a description of a changing ecosystem. *Hydrobiologia* 540(1–3):1–11
- Mitchener H, Torfs H (1996) Erosion of mud/sand mixtures. *Coast Eng* 29:1–25
- Mulder HP, Udink C (1990) Modelling of cohesive sediment transport. A case study: the western Scheldt estuary. *Coastal Engineering Proceedings*, 1(22)
- Nihoul JCJF, Ronday F, Peters JJ, Sterling A (1978) Hydrodynamics of the Scheldt estuary. In: Nihoul JCJF (ed) *Hydrodynamics of estuaries and fjords*. Elsevier, Amsterdam, pp 27–53
- Nikuradse J (1933) Laws of flow in rough pipes. NACA Tech. Mem., No.1292 (translation, 1950), Washington, 62 pp.
- Panagiotopoulos I, Voulgaris G, Collins MB (1997) The influence of clay on the threshold of movement of fine sandy beds. *Coast Eng* 32(1): 19–43
- Peters (1975) Les mecanismes de mélange des eaux dans l'estuaire de l'Escaut. *Tijdschrift der Openbare Werken van België* 2, pp. 101–119
- Portela LI, Neves R (1994) Numerical modelling of suspended sediment transport in tidal estuaries: a comparison between the Tagus (Portugal) and the Scheldt (Belgium–The Netherlands). *Neth J Aquat Ecol* 28(3–4):329–335
- Prandtl L (1925) Bericht über untersuchungen zur ausgebildeten turbulenz. *ZAMM* 5:136–139
- Smagorinsky J (1963) General circulation experiments with the primitive equations: I. The basic experiment. *Mon Weather Rev* 91(3):99–164
- Toorman EA (2000) Numerical simulation of turbulence damping in sediment-laden flow. Part 2. Suspension capacity of uniform turbulent shear flows. Report HYD/ET/00/COSINUS4, Hydraulics Laboratory, K.U.Leuven, 23 pp
- Toorman EA (2002) Modelling of turbulent flow with cohesive sediment. In: Winterwerp JC, Kranenburg C (eds) *Proceedings in Marine Science*, vol 5: Fine sediment dynamics in the marine environment. Elsevier Science, Amsterdam, pp 155–169
- Toorman EA (2003) Validation of macroscopic modelling of particle-laden turbulent flows. *Proceedings 6th Belgian National Congress on Theoretical and Applied Mechanics* (Gent, 26–27 May 2003), CD Rom, 7 pp
- Toorman E A (2011) Low-Reynolds modelling of high-concentrated near-bottom suspended sediment transport. IAHR Symposium on Two-phase Modelling for Sediment Dynamics in Geophysical Flows (THESIS-2011, Paris, April 26–28, 2011), Abstract, 4 pp
- Toorman E, Bi Q (2011) Dealing with benthic high-concentrated layers and fluid mud in cohesive sediment transport modeling. INTE RCOH'11. Book of Abstracts. Int. Conf. on Cohesive Sediment Transport Processes. Shanghai, China, 18–21 October 2011, 85–86
- Toorman E, Bi Q (2012) Section 2.4, EU FP7 FIELD\_AC Report D3.3. In: Liste M, Monbaliu J (Eds) *Improvements to sea-bed boundary conditions* (pp. 19–31)
- Toorman E, Bi Q (2013a). Hybrid two-phase/mixture modelling of sediment transport. Abstracts THESIS-2013 (CDRom). Symposium on Two-phase Modelling for Sediment Dynamics. Chatou (France), 10–12 June 2013, 4 pp
- Toorman E, Bi Q (2013b) A practical model for drag modulation by suspended sediment, with application to the Scheldt estuary. INTE RCOH2013 Book of Abstracts. Int. Conf. on Cohesive Sediment Transport. Gainesville, Florida, 20–24 October 2013, 7–8
- Toorman E, Bi Q (2013c). Hybrid two-phase/mixture modelling of sediment transport as a tool for large-scale morphological model development. *Advances in Water Resources* (SI THESIS2013)
- Van Driest ER (1956) On turbulent flow near a wall. *J. Aeronautical Science*, 23, 1007-1011+1136
- Van Kessel T, Vanlede J (2010) Impact of harbour basins on mud dynamics Scheldt estuary in the framework of LTV. Delft, Deltares, p 29
- Van Kessel T, Vanlede J, & Bruens A (2006) Development of a mud transport model for the Scheldt estuary in the framework of LTV. Report Z4210 WL| Delft Hydraulics and Flanders Hydraulics Research, Delft
- Van Kessel T, Vanlede J, de Kok J (2011) Development of a mud transport model for the Scheldt estuary. *Cont Shelf Res* 31:S165–S181
- Van Rijn LC (1984) Sediment transport, part I: bed load transport. *J Hydraul Eng* 110(10):1431–1456
- Van Rijn LC (1993) Principles of sediment transport in rivers, estuaries and coastal seas, vol 2, no 3. Aqua publications, Amsterdam, p 4



- Verbeek H, Jansen, MHP, & Wouters CAH (1998) Adaptation of 2D sediment transport patterns using 3D hydrodynamic modelling. In OCEANS'98 Conference Proceedings (Vol. 1, 444–448), IEEE
- Verlaan PAJ, Donze M, Kuik P (1998) Marine vs fluvial suspended matter in the Scheldt estuary. *Estuar Coast Shelf Sci* 46(6):873–883
- Waeles B (2005) Detachment and transport of silt sand gravel mixtures by channel flows. PhD thesis. University of Caen Caen, France
- Waeles B, Le Hir P, Lesueur P, Delsinne N (2007) Modelling sand/mud transport and morphodynamics in the Seine river mouth (France): an attempt using a process-based approach. *Hydrobiologia* 588(1):69–82
- Wartel S. & van Eck, GTM (2000) Slibhuishouding van de Schelde. Report, Koninklijk Belgisch Instituut voor Natuurwetenschappen (Brussels) & Rijksinstituut der Kust en Zee (Middelburg, NL), 66 pp. (in Dutch)
- Widera P, Toorman E, Lacor C (2009) Large eddy simulation of sediment transport in open-channel flow. *J Hydraul Res* 47(3):291–298